

# Total Suppression of High-Frequency Transient Oscillations in Dual-Active-Bridge Series-Resonant Converter by Trajectory-Switching Modulation

Chuan Sun , Graduate Student Member, IEEE, Xingyue Jiang , Lingling Cao , Member, IEEE, and K. H. Loo , Member, IEEE

**Abstract**—Dual-active-bridge series-resonant converter (DAB-SRC) is increasingly used in many emerging power electronics applications requiring fast dynamic responses. However, under conventional transient phase-shift modulation strategy, DAB-SRC generally suffers from large-amplitude transient oscillations when its phase-shift angle is changed abruptly by a high-gain controller. These oscillations occur at the beat frequency, which results from the interaction between the switching-frequency and resonant-frequency components in the series-resonant tank during transient states. Besides incurring high voltage and current stresses on the power-stage devices, these transient oscillations also span many switching cycles between the original and new steady states and cause perturbations to the output voltage of DAB-SRC, thereby degrading its dynamic performance and output voltage quality. To mitigate these problems, a new transient modulation strategy, known as trajectory-switching modulation (TSM), is proposed for achieving an accurate and computationally efficient trajectory planning of the resonant voltages and currents of DAB-SRC during transient states, and its basic operation is to govern the transient switching patterns of the gating signals according to a simple set of closed-form equations. The proposed TSM strategy can guarantee convergence to the next new steady state within about one switching cycle and avoid needing costly sensors and complex computation for implementation, and it is inherently compatible with high-gain controllers for realizing oscillation-free fast dynamic responses.

**Index Terms**—Dual-active-bridge (DAB) converter, dynamic response, phase-shift modulation, series-resonant converter, transient oscillations.

## NOMENCLATURE

$V_1, V_2$	Input and output voltages.
$J, \nabla J$	Cost function and its gradient.
$V_{2,\text{ref}}$	Output reference voltage.

Manuscript received May 22, 2021; revised August 20, 2021 and November 12, 2021; accepted December 20, 2021. Date of publication December 24, 2021; date of current version February 18, 2022. This work was supported by PolyU Postdoctoral Fellowships Scheme under Project YW4X. Recommended for publication by Associate Editor Y. Siwakoti. (Corresponding author: Lingling Cao.)

Chuan Sun, Xingyue Jiang, and K. H. Loo are with the Department of Electronic and Information Engineering, The Hong Kong Polytechnic University, 999077 Hong Kong, China (e-mail: chuan.sun@connect.polyu.hk; xingyue.jiang@connect.polyu.hk; kh.loo@polyu.edu.hk).

Lingling Cao is with the School of Mechanical Engineering and Automation, Harbin Institute of Technology, Shenzhen 518055, China (e-mail: caolinling@hit.edu.cn).

Color versions of one or more figures in this article are available at <https://doi.org/10.1109/TPEL.2021.3138150>.

Digital Object Identifier 10.1109/TPEL.2021.3138150

$v_e[n]$	Output error voltage.
$P$	Transferred power.
$C_o$	Output capacitance.
$R_L$	Load resistance.
$L_r$	Resonant inductance.
$C_r$	Resonant capacitance.
$R_r$	Lumped resistance.
$N : 1$	Transformer's turns ratio.
$i_r$	Resonant tank current.
$i_2$	Terminal current of secondary-side bridge.
$I_{RL}$	Load current.
$v_{Lr}$	Voltage across $L_r$ .
$v_{Cr}$	Voltage across $C_r$ .
$v_{LC}$	Voltage across the $L_r-C_r$ network.
$v_{ab}, v_{cd}$	Two-level square-wave voltages.
$\alpha, \alpha[n]$	Phase-shift angle.
$\delta$	Phase-shift increment or decrement.
$\beta$	Transient phase-shift angle.
$\varphi$	Transient pulselwidth of $v_{ab}$ or $v_{cd}$ .
$\omega_s$	Angular switching frequency.
$\omega_r$	$= 1/(\sqrt{L_r C_r})$ . Angular resonant frequency.
$f_s$	$= \omega_s/(2\pi)$ . Switching frequency.
$T_s$	$= 1/f_s$ . Switching period.
$f_r$	$= \omega_r/(2\pi)$ . Resonant frequency.
$F$	$= f_s/f_r$ . Normalized frequency.
$z_r$	$= \sqrt{L_r/C_r}$ . Characteristic impedance.
$X_r$	$= \omega_s L_r - 1/(\omega_s C_r)$ . Equivalent impedance.
$\theta$	$= \omega_s t$ . Angular displacement at time $t$ .

## I. INTRODUCTION

Due to a number of attractive benefits (e.g., ease of modulation, high density, and high efficiency),  $LC$ -type dual-active-bridge (DAB) series-resonant converter (DAB-SRC) is a highly competitive candidate used in high-power bidirectional dc–dc applications such as energy storage systems [1]. In order to improve its steady-state performance, some multidegree-of-freedom modulation strategies have been proposed in [2]–[5] aiming to achieve minimum-resonant-current operation, extension of zero-voltage switching (ZVS) region, reduction of backflow power, improvement of overall conversion efficiency, etc. However, a careful literature survey on improving its transient performance indicates that the previous works are mainly

focused on feedback control design, while the transient properties of DABSRC and transient modulation strategies are rarely discussed. In order to further optimize the transient performance of DABSRC and to ensure reliable operation under large-amplitude external disturbances such as pulsating loads [6], there is an imminent need to acquire an in-depth understanding of converter's transient behavior and its relation to the transient modulation strategy.

The widely used control methods for DAB converters are proportional–integral (PI) based single-loop voltage control [7] and dual-loop current control [8], [9]. However, although the small-signal dynamic models established in [10]–[12] can help to tune the PI controller, the interaction between the two tuning parameters makes it difficult to simultaneously achieve fast and stable performance over the entire operating range. The peak-current-mode feedforward control solutions proposed in [13] and [14] have better dynamic performance, but the high-frequency (HF) inductor current must be sampled at least twice the switching frequency. Thus, the utility of such methods is quite limited, particularly in HF-operated DAB converters. Recently, advanced model predictive control (MPC) has been applied by researchers to achieve fast transient response in both non-resonant DAB converter [6], [15] and DABSRC [16]. Fast transient response allows the use of smaller output capacitors, thereby reducing the requirement and volume of output filters, and helps to alleviate the reliability problems associated with the use of electrolytic capacitors. However, in exchange for fast transient response, the feedback controller's gain and bandwidth must be increased, resulting in larger step changes of the control variable, i.e., phase-shift angle.

In fact, a converter's transient response is also heavily affected by the transient modulation strategy when updating the control variable(s). It has been observed that a sudden change in phase-shift angle can lead to an excessive transient dc bias in the inductor current of nonresonant DAB converter [17]. Similarly, for DABSRC, the conventional transient single-phase-shift modulation (CT-SPSM) can cause a rapid change of the voltage applied to the series-resonant tank, thereby leading to HF transient oscillations in the tank's voltages and currents. In practice, such HF transient oscillations will decay to zero due to the presence of equivalent series resistance, but the settling time may be orders of magnitude longer than a switching cycle. Also, the typically large peak-to-peak amplitudes of the transient tank's voltages and currents can result in high transient voltage and current stresses on the circuit components, which will degrade their long-term reliability or expose the components to premature failures.

To further improve the transient performance of DAB converter, an important and fast-growing research theme is to design suitable transient switching patterns that will drive the converter's voltages and currents to change according to some predefined trajectories during transient states. For nonresonant DAB converter, some optimized transient phase-shift modulation strategies have been successfully proposed in [17]–[19] which can achieve a dynamic volt-second balance in the energy transfer inductor, thus enabling the inductor current to smoothly reach a new steady state within one switching cycle under load

power changes. It is believed that the transient trajectories of the resonant voltages and currents in DABSRC can also be shaped by suitably designed the transient switching patterns. However, unlike the piecewise-linear inductor current in conventional single-inductor DAB converter, the resonant current in DABSRC is a nonlinear function of phase-shift angle (control variable) and cannot be immediately clamped because of the inertia of the resonant network. Due to the inherent differences in circuit characteristics, none of the previously proposed transient modulation strategies are effective in attenuating HF transient oscillations in DABSRC. In a closely related study [20], a method known as “trajectory-prediction-based power transient control” can be applied to suppress HF transient oscillations in DABSRC, as it is able to actively alter the trajectory of the resonant current. Unfortunately, this method was only validated in open-loop conditions, possibly due to the high complexity of its modulation law. Besides, similar to most existing state-plane trajectory control methods that are proposed for other converter topologies [21]–[26], a common drawback associated with them is that rich feedback information and hence many sensors are required for the trajectory planning and computation. This makes them complex and costly to implement and also sensitive to noise and measurement errors. So far, there seems to be no simple and accurate transient modulation strategy reported in the literature that can eliminate HF transient oscillations in a real-time closed-loop controlled DABSRC.

To fill this gap, a novel trajectory-switching modulation (TSM) strategy is proposed in this article. To verify its advantages over CT-SPSM, the transient performances under both modulation strategies when applied to an MPC-controlled DABSRC are presented and compared, and their simulation and experimental results are systematically analyzed. The merits of the proposed method and the main contributions of this article can be summarized as follows.

- 1) It is compatible with fast and large-amplitude changes in the phase-shift angle of DABSRC, enabling it to swiftly reach a new steady state (ideally within about one switching cycle) following the external disturbances without inducing noticeable HF transient oscillations.
- 2) Unlike existing trajectory control methods, no voltage and current information is required for the implementation of the proposed method, thus eliminating the need for additional costly high-bandwidth sensors.
- 3) This article presents the first practical demonstration of the *closed-loop* implementation of transient modulation strategy in DABSRC and its effectiveness in suppressing HF transient oscillations.
- 4) Unlike the existing feedback control designs with which control bandwidth must be limited to prevent the occurrence of HF transient oscillations, the elimination of such oscillations by the proposed method enables the implementation of high-gain, high-bandwidth fast controller in DABSRC to achieve superior transient performance.

The rest of this article is organized as follows. Section II describes the basic operation of SPSM. The principle of operation of the proposed TSM strategy is presented in Section III. In Section IV, detailed analyses in system modeling and MPC

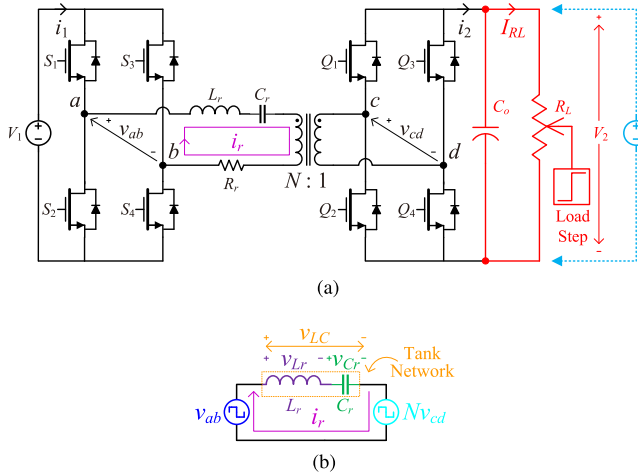


Fig. 1. Dual-active-bridge series-resonant converter (DABSRC). (a) Power Stage. (b) AC equivalent circuit.

controller design are presented, followed by simulations and experimental results in Section V. Finally, Section VI concludes this article.

## II. BASIC OPERATION OF SPSM

### A. Circuit Description

Fig. 1(a) shows the power stage of a DABSRC, which consists of two full-bridge converters, a series-resonant network  $L_r - C_r - R_r$ , and a HF transformer. The transformer's magnetizing inductance is assumed to be very large. The inductance of  $L_r$  is composed of the transformer's leakage inductance and an auxiliary inductance.  $R_r$  is a lumped resistance, which includes the ON-state resistances of power switches, resistances of PCB tracks, winding resistances of magnetic components, etc. In practice, the condition  $R_r^2 \ll 4L_r/C_r$  generally holds true, hence the effect of  $R_r$  can be neglected. Therefore, the ac equivalent circuit of DABSRC [see Fig. 1(b)] is generally second-order and underdamped. Since  $R_r$  is small, the high- $Q$  resonant network is effective in suppressing higher harmonics from the ac-link voltages (i.e.,  $v_{ab}$  and  $v_{cd}$ ), thus producing an approximately sinusoidal resonant tank current  $i_r$ . On the transformer's secondary side,  $i_r$  is rectified to produce  $i_2$  which is smoothed by the output filter capacitor  $C_o$  to produce a dc load current  $I_{RL}$ .

### B. Steady-State Operation of SPSM

Single-phase-shift modulation (SPSM) is the simplest and most commonly used modulation method for DABSRC. The steady-state operation of SPSM can be explained by referring to the waveforms shown in Fig. 2. To prevent short-circuit, the two switches belonging to a bridge leg (i.e.,  $\{S_1, S_2\}$ ,  $\{S_3, S_4\}$ ,  $\{Q_1, Q_2\}$ , and  $\{Q_3, Q_4\}$ ) are switched complementarily with a duty ratio of 50% at a fixed frequency. Since the dead time is typically much shorter than one switching period, it is ignored in the following analysis. Diagonal switches (i.e.,  $\{S_1, S_4\}$ ,  $\{S_2, S_3\}$ ,  $\{Q_1, Q_4\}$ , and  $\{Q_2, Q_3\}$ ) are switched synchronously to

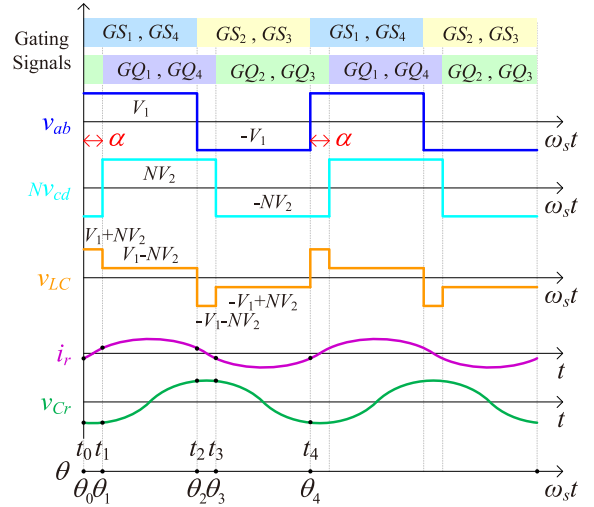


Fig. 2. Steady-state waveforms of DABSRC under SPSM.

produce square-wave voltages  $v_{ab}$  and  $v_{cd}$ , across the primary-side and secondary-side full bridges, respectively. It can be seen that  $\alpha$  determines the waveform of  $v_{LC}$ , thus controlling the direction and amount of the transmission power of DABSRC. When  $\alpha > 0$ , the net power flow is from the input voltage source  $V_1$  to the load  $R_L$ , which is defined as forward power flow. When  $\alpha < 0$  and the load  $R_L$  is replaced by a dc voltage source  $V_2$ , reverse power flow, from  $V_2$  to  $V_1$ , can also be achieved.

Referring to Fig. 1(b), the  $L_r - C_r$  series-resonant network is excited by a multilevel voltage  $v_{LC} = v_{ab} - Nv_{cd}$ . Applying Kirchhoff's voltage law (KVL) to the equivalent circuit in Fig. 1(b) yields

$$\begin{aligned} v_{LC} &= L_r \frac{di_r(t)}{dt} + \frac{1}{C_r} \int_0^t i_r(t) dt + v_{Cr}(0) \\ \Rightarrow 0 &= L_r \frac{d^2 i_r(t)}{dt^2} + \frac{1}{C_r} i_r(t). \end{aligned} \quad (1)$$

To solve (1),  $i_r$  can be generally assumed to have the following form:

$$i_r(t) = A_i \cos(\omega_r(t - t_i)) + B_i \sin(\omega_r(t - t_i)) \quad (2)$$

or

$$i_r\left(\frac{\theta}{\omega_s}\right) = A_i \cos \frac{\theta - \theta_i}{F} + B_i \sin \frac{\theta - \theta_i}{F} \quad (3)$$

for  $t$  in the time interval  $[t_i, t_{i+1}]$ , where  $A_i$  and  $B_i$  are constants to be determined.  $\theta_i = \omega_s t_i$  is the angular displacement at time  $t_i$ , where  $i = 1, 2, 3, \dots$  indicates the  $i$ th trajectory-switching point.

Substituting (3) into (1) gives

$$\begin{aligned} v_{Cr}\left(\frac{\theta}{\omega_s}\right) &= \frac{1}{C_r} \int_0^t i_r(t) dt + v_{Cr}(0) \\ &= v_{LC} - \left( -A_i \sin \frac{\theta - \theta_i}{F} + B_i \cos \frac{\theta - \theta_i}{F} \right) Z_r. \end{aligned} \quad (4)$$

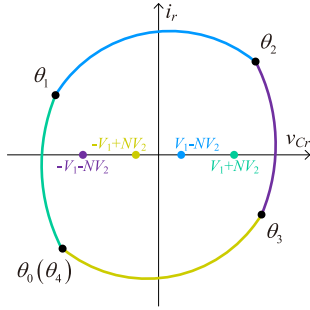


Fig. 3. Steady-state state-plane diagram of DABSRC under SPSM.

$A_i = i_r(\theta_i/\omega_s)$  and  $B_i = (v_{LC} - v_{Cr}(\theta_i/\omega_s))/Z_r$  are obtained by letting  $\theta = \theta_i$  in (3) and (4), which gives the general analytical expressions of  $i_r$  and  $v_{Cr}$  as

$$i_r\left(\frac{\theta}{\omega_s}\right) = i_r\left(\frac{\theta_i}{\omega_s}\right) \cos \frac{\theta - \theta_i}{F} + \frac{v_{LC} - v_{Cr}\left(\frac{\theta_i}{\omega_s}\right)}{Z_r} \sin \frac{\theta - \theta_i}{F} \quad (5)$$

$$\begin{aligned} v_{Cr}\left(\frac{\theta}{\omega_s}\right) &= v_{LC} \cdot \left(1 - \cos \frac{\theta - \theta_i}{F}\right) + v_{Cr}\left(\frac{\theta_i}{\omega_s}\right) \cos \frac{\theta - \theta_i}{F} \\ &\quad + Z_r \cdot i_r\left(\frac{\theta_i}{\omega_s}\right) \sin \frac{\theta - \theta_i}{F}. \end{aligned} \quad (6)$$

The sine and cosine terms in (5) and (6) can be combined by using trigonometric identities to give (7), which indicates that the 2-D state-plane diagram shown in Fig. 3 is graphically described by piecewise circular arcs

$$\begin{aligned} Z_r^2 i_r^2 \left(\frac{\theta}{\omega_s}\right) + \left(v_{Cr}\left(\frac{\theta}{\omega_s}\right) - v_{LC}\right)^2 \\ = Z_r^2 i_r^2 \left(\frac{\theta_i}{\omega_s}\right) + \left(v_{Cr}\left(\frac{\theta_i}{\omega_s}\right) - v_{LC}\right)^2. \end{aligned} \quad (7)$$

Due to the steady-state operation of SPSM, the waveforms of  $i_r$  and  $v_{Cr}$  are symmetrical comprising four distinct time intervals in one switching cycle. It can be observed from Fig. 3 that point  $\theta_0(\theta_4)$  and point  $\theta_2$  are symmetrical about the origin, so as point  $\theta_1$  and point  $\theta_3$ . Hence

$$\begin{cases} i_r\left(\frac{\theta_0}{\omega_s}\right) = -i_r\left(\frac{\theta_2}{\omega_s}\right), v_{Cr}\left(\frac{\theta_0}{\omega_s}\right) = -v_{Cr}\left(\frac{\theta_2}{\omega_s}\right) \\ i_r\left(\frac{\theta_1}{\omega_s}\right) = -i_r\left(\frac{\theta_3}{\omega_s}\right), v_{Cr}\left(\frac{\theta_1}{\omega_s}\right) = -v_{Cr}\left(\frac{\theta_3}{\omega_s}\right). \end{cases} \quad (8)$$

By substituting (8) into (5) and (6), the values of  $i_r(\theta_i/\omega_s)$  and  $v_{Cr}(\theta_i/\omega_s)$  at different trajectory-switching points  $\theta_i$  can be solved exactly. For example,

$$i_r\left(\frac{\theta_0}{\omega_s}\right) = \frac{1}{Z_r} \left[ NV_2 \sec\left(\frac{\pi}{2F}\right) \sin\left(\frac{\pi - 2\alpha}{2F}\right) - V_1 \tan\left(\frac{\pi}{2F}\right) \right] \quad (9)$$

$$v_{Cr}\left(\frac{\theta_0}{\omega_s}\right) = NV_2 \left[ 1 - \cos\left(\frac{\alpha}{F}\right) - \sin\left(\frac{\alpha}{F}\right) \tan\left(\frac{\pi}{2F}\right) \right] \quad (10)$$

and other instantaneous values of  $i_r$  and  $v_{Cr}$  at any time can be obtained accordingly.

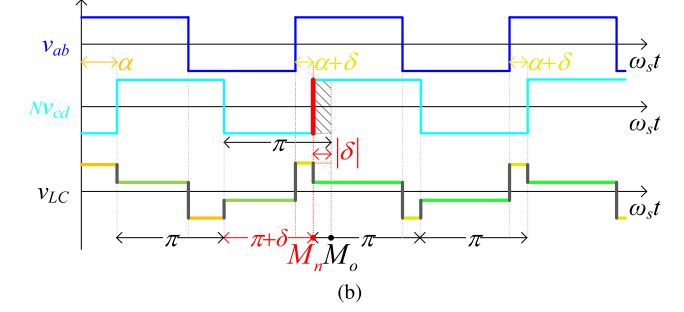
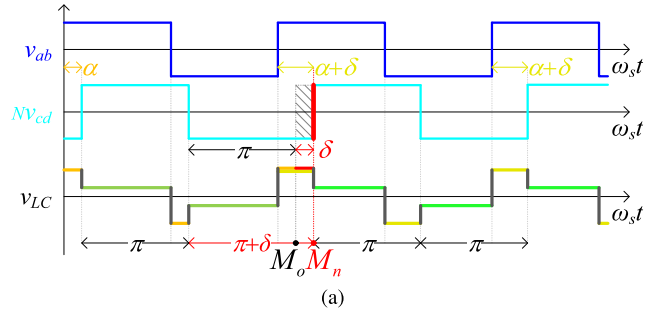


Fig. 4. Conventional transient-state operation of SPSM (CT-SPSM) for (a)  $\delta > 0$  and (b)  $\delta < 0$ .

### C. Transient-State Operation of SPSM

During transient states, the phase-shift angle of DABSRC is generally updated from its initial value  $\alpha$  in the current cycle to  $\alpha + \delta$  before the end of the next switching cycle, where  $\delta$  is the angle increment or decrement. However, there is no standard implementation method for updating the phase-shift angle and it mainly depends on how a pulsewidth modulation (PWM) modulator is implemented in a microprocessor. The most conventional transient-state operation of SPSM (i.e., CT-SPSM) is illustrated in Fig. 4, where the transient low-level duration of  $v_{cd}$  will be increased ( $\delta > 0$ ) or decreased ( $\delta < 0$ ) by  $|\delta|$ , i.e., the turn-ON instances of  $Q_1$  and  $Q_4$  are adjusted from point  $M_o$  to point  $M_n$ , in order to realize a desired new phase-shift angle  $\alpha + \delta$ .

Despite its popularity, the impact of CT-SPSM on the transient behavior of DABSRC, however, has not been thoroughly investigated in the literature. To better examine the large-scale transient behavior of DABSRC under CT-SPSM, open-loop simulations (with both sides of the converter connected to dc voltage sources and other converter parameters specified in Table I) were performed on Powersim (PSIM) software, and the results are presented in Fig. 5. In Fig. 5(a) and (b), the converter is operated in forward power modes; in Fig. 5(c), the direction of power flow changes from the forward mode to the reverse mode.

It is evident from the simulation results shown in Fig. 5 that CT-SPSM generally leads to large-amplitude HF transient oscillations which exist in all resonant tank voltage and current waveforms (e.g.,  $i_r$ ,  $v_{Cr}$ , and  $v_{Lr}$ ). The oscillations are caused by the excitation of the resonant tank by a step change in  $v_{LC}$  resulting from a step increase or decrease of the low-level duration of  $v_{cd}$ . Since the resonant tank will absorb or release abundant

TABLE I  
HARDWARE SPECIFICATIONS AND SIMULATION PARAMETERS USED

Item	Description
Rated Output Power $P_{max}$	250 W
Input Voltage $V_1$	100 V
Output Voltage $V_2$	100 V
Output Capacitance $C_o$	47 $\mu\text{F}$
Load Resistance $R_L$	100/45 $\Omega$
Transformer Turns Ratio $N : 1$	1 : 1
Resonant Inductance $L_r$	321 $\mu\text{H}$
Equivalent series resistance of $L_r$	211 m $\Omega$
Resonant Capacitance $C_r$	45 nF
Resonant Frequency $f_r$	41.8756 kHz
Switching Frequency $f_s$	50 kHz
Dead Time	300 ns
Switches $S_1 \sim S_4$ and $Q_1 \sim Q_4$	UnitedSiC UJC06505K
Drain-Source ON Resistance	45 m $\Omega$
Gate Driver	TI UCC21520
Op Amp for ADC	TI TL082
Voltage Transducer	Two-Resistor Voltage Divider
Current Transducer	LEM LA 55-P
Microprocessor	TI TMS320F28335
Simulation Software	PSIM 12.0.4

energy at that transient moment, the periodic tank-energy balance will be broken suddenly. Taking the frequency spectrum of the transient resonant current  $i_r$ , as shown in Fig. 6, reveals that it contains an additional component at the resonant frequency  $f_r$  which is superimposed with the dominant component at the switching frequency  $f_s$ . The switching frequency component is known to originate from the forced response of the second-order  $L_r - C_r - R_r$  resonant tank due to the terminal voltages  $v_{ab}$  and  $v_{cd}$ , while the resonant frequency component emerges from the natural response of the resonant tank when excited by a step change in  $v_{LC}$ .

By the effect of the beat phenomenon, the superposition of the two sinusoidal components produces a resultant wave with an envelope that fluctuates at the beat frequency  $f_B = f_s - f_r$  [27]. For all the simulated cases shown in Fig. 5, the switching frequency  $f_s$  and the resonant frequency  $f_r$  are 50 and 41.8 kHz, respectively, hence the theoretical beat frequency is 8.2 kHz, which closely matches with the frequency of the envelopes of the simulated transient waveforms. For a second-order  $L_r - C_r - R_r$  resonant circuit, its natural response will decay exponentially with a time constant  $2L_r/R_r$ , accompanied by a decaying amplitude of the envelope, as the short-lived burst of energy is dissipated by  $R_r$ .

It should be noted a large step change in  $\delta$  will lead to large-amplitude HF transient oscillations which will impose high voltage and current stresses on all the power stage components of DABSRCS, and may even damage them. These oscillations reflect the main drawback of CT-SPSM and the problem is typically avoided by gradually updating the phase-shift angle so that the phase-shift angle is varied by a small increment/decrement between two consecutive switching cycles. Clearly, this is not a desirable solution as it leads to slow converter's dynamic

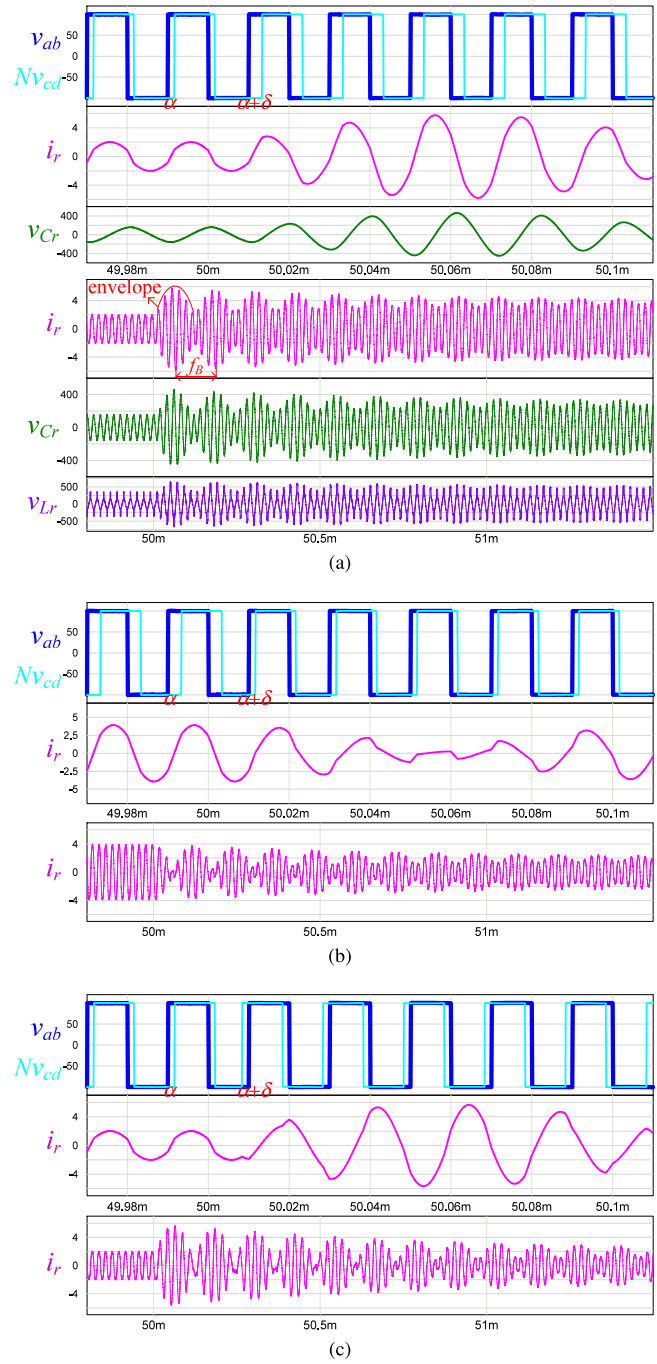


Fig. 5. Simulated transient responses under CT-SPSM. (a) Step-load increase:  $\alpha = \pi/6$ ,  $\delta = \pi/6$ , and  $\alpha + \delta = \pi/3$ . (b) Step-load decrease:  $\alpha = \pi/3$ ,  $\delta = -\pi/6$ , and  $\alpha + \delta = \pi/6$ . (c) Step change of power flow direction:  $\alpha = \pi/6$ ,  $\delta = -\pi/3$ , and  $\alpha + \delta = -\pi/6$ .

response. The problem must be mitigated by designing a new transient-state modulation method.

### III. PROPOSED TRAJECTORY-SWITCHING MODULATION STRATEGY FOR DABSRCS

As the impedance, and hence the natural response, of the resonant tank usually cannot be altered, a more effective method for the suppression of HF transient oscillations is to modify

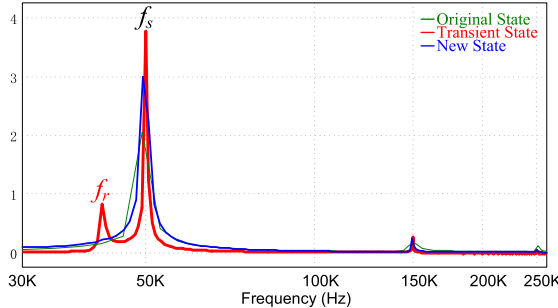


Fig. 6. Frequency spectrum of resonant current  $i_r$  under different states.

the resonant tank's forced response by actively shaping its input excitation ( $v_{LC}$ ) with an appropriate transient switching sequence. The following subsections will describe the designs of the proposed transient switching sequences for the cases of increasing and decreasing power in Figs. 7 and 8, respectively. The superscript associated with the phase angle  $\theta$ , e.g., “I” in  $\theta_0^I$ , is used to denote the operation mode under TSM.

#### A. Increasing Power ( $\delta > 0$ )

The case of  $\delta > 0$  corresponds to an increase of power. By referring to an example of updating a positive value of  $\delta$  under TSM, as shown in Fig. 7(a), there are two modulation parameters involved, i.e., the transient phase-shift angle ( $\beta_1$ ) between  $v_{ab}$  and  $v_{cd}$  and the positive pulse width ( $\varphi_1$ ) of  $v_{cd}$ , which can be adjusted during transient state to alter the trajectories of  $v_{Cr}$  and  $i_r$  while  $v_{ab}$  is kept unchanged as a 50% duty-cycle square wave. Both parameters,  $\beta_1$  and  $\varphi_1$ , are modulated via a multistep process during each switching cycle to update the phase-shift angle from the original steady-state value  $\alpha$  to the new steady-state value  $\alpha + \delta$ . By means of a multistep updating process, a sudden surge of injected energy to the resonant tank is therefore prevented. On the contrary, for CT-SPSM, as previously depicted in Fig. 4, only the transient phase-shift angle is modulated (i.e.,  $\beta_1 = \alpha + \delta$ ) while the duty cycle of  $v_{cd}$  is always kept as 0.5, which causes a sudden injection of energy to the resonant tank that triggers the undesirable HF transient oscillations.

According to [22], the instantaneous tank energy ( $e_T$ ) is given by  $e_T = (C_r v_{Cr}^2 + L_r i_r^2)/2$ , which is proportional to the square of the radius of the state-plane trajectory associated with the current state. The underlying principle of TSM can be explained by referring to the state-plane diagram shown in Fig. 7(b). Since  $e_T$  can be modified by modulating  $\beta_1$  and  $\varphi_1$ , i.e., by turning ON and OFF the secondary-side switches in appropriate ways, the transient trajectories of  $i_r$  and  $v_{Cr}$  should accordingly be altered in a deterministic way (by modulating  $\beta_1$  and  $\varphi_1$ ) to enable them to acquire their new steady-state trajectories at a specified time, e.g., at the end of one switching cycle, and once they enter the new state trajectories (without oscillation), they should remain there until the next transient event/command occurs. If  $i_r$  and  $v_{Cr}$  can reach their new steady states in one switching cycle, oscillations are eliminated and settling time is shortened significantly. Therefore, in order to eliminate HF transient oscillations, the boundary values of  $v_{Cr}$

and  $i_r$  at the beginning and the end of the transient process, i.e.,  $\theta_4^I/\omega_s$  and  $\theta_8^I/\omega_s$ , should be equal to their original and new steady-state values corresponding to the phase-shift angle  $\alpha$  and  $\alpha + \delta$ , respectively. This can be achieved by finding the solutions for  $\beta_1$  and  $\varphi_1$  that satisfy the boundary conditions at  $\theta_4^I/\omega_s$  and  $\theta_8^I/\omega_s$ . Once these solutions are found, an optimal transient switching sequence (as well as transient state-plane trajectories) can be constructed that completes the transient process in one switching cycle.

Under TSM, the transient process which begins at  $\theta_4^I/\omega_s$  and ends at  $\theta_8^I/\omega_s$  can be divided into four intervals, namely,  $\theta_5^I - \theta_4^I = \beta_1$ ,  $\theta_6^I - \theta_5^I = \pi - \beta_1$ ,  $\theta_7^I - \theta_6^I = \beta_1 + \varphi_1 - \pi$ , and  $\theta_8^I - \theta_7^I = 2\pi - \beta_1 - \varphi_1$ . It is assumed that the terminal voltages  $V_1$  and  $V_2$  are constant during the transient process, which is reasonable given the very short duration, i.e., one switching cycle, of the transient process. To determine the instantaneous values of  $v_{Cr}$  and  $i_r$  at the intermediate points between  $\theta_4^I/\omega_s$  and  $\theta_8^I/\omega_s$ , i.e.,  $i_r(\theta_5^I/\omega_s) \sim i_r(\theta_8^I/\omega_s)$  and  $v_{Cr}(\theta_5^I/\omega_s) \sim v_{Cr}(\theta_8^I/\omega_s)$ , (5) and (6) are applied to an iterative manner. The lower boundary values can be found from the original steady-state values  $i_r(\theta_4^I/\omega_s) = i_r(\theta_0^I/\omega_s)$  and  $v_{Cr}(\theta_4^I/\omega_s) = v_{Cr}(\theta_0^I/\omega_s)$  from (9) and (10), respectively. The upper boundary values can be found after four iterations as

$$\begin{aligned} i_r\left(\frac{\theta_8^I}{\omega_s}\right) = & -\frac{4NV_2}{Z_r} \cos\left(\frac{2\beta_1 + \varphi_1 - 4\pi}{2F}\right) \sin\left(\frac{\varphi_1}{2F}\right) \\ & + \frac{NV_2}{Z_r} \sec\left(\frac{\pi}{2F}\right) \sin\left(\frac{5\pi - 2\alpha}{2F}\right) - \frac{V_1}{Z_r} \tan\left(\frac{\pi}{2F}\right) \end{aligned} \quad (11)$$

$$\begin{aligned} v_{Cr}\left(\frac{\theta_8^I}{\omega_s}\right) = & 4NV_2 \sin\left(\frac{2\beta_1 + \varphi_1 - 4\pi}{2F}\right) \sin\left(\frac{\varphi_1}{2F}\right) \\ & + NV_2 \left[ 1 - \sec\left(\frac{\pi}{2F}\right) \cos\left(\frac{5\pi - 2\alpha}{2F}\right) \right]. \end{aligned} \quad (12)$$

As the objective is to eliminate HF transient oscillations,  $i_r(\theta_8^I/\omega_s)$  and  $v_{Cr}(\theta_8^I/\omega_s)$  must be equal to their new steady-state values at  $\theta_{12}^I/\omega_s$ . Hence

$$\begin{aligned} i_r\left(\frac{\theta_8^I}{\omega_s}\right) = & i_r\left(\frac{\theta_{12}^I}{\omega_s}\right) \\ = & \frac{1}{Z_r} \left[ NV_2 \sec\left(\frac{\pi}{2F}\right) \sin\left(\frac{\pi - 2\alpha - 2\delta}{2F}\right) - V_1 \tan\left(\frac{\pi}{2F}\right) \right] \end{aligned} \quad (13)$$

$$\begin{aligned} v_{Cr}\left(\frac{\theta_8^I}{\omega_s}\right) = & v_{Cr}\left(\frac{\theta_{12}^I}{\omega_s}\right) \\ = & NV_2 \left[ 1 - \cos\left(\frac{\alpha + \delta}{F}\right) - \sin\left(\frac{\alpha + \delta}{F}\right) \tan\left(\frac{\pi}{2F}\right) \right] \end{aligned} \quad (14)$$

which are obtained by replacing  $\alpha$  by  $\alpha + \delta$  in both (9) and (10).

Combining (11) with (13), and (12) with (14), gives

$$\sec\frac{\pi}{2F} \sin\frac{2\pi + \delta}{2F} \cos\frac{2\alpha + \delta - 3\pi}{2F} = 2\sin\frac{\varphi_1}{2F} \cos\frac{2\beta_1 + \varphi_1 - 4\pi}{2F} \quad (15)$$

$$\sec\frac{\pi}{2F} \sin\frac{2\pi + \delta}{2F} \sin\frac{2\alpha + \delta - 3\pi}{2F} = 2\sin\frac{\varphi_1}{2F} \sin\frac{2\beta_1 + \varphi_1 - 4\pi}{2F}. \quad (16)$$

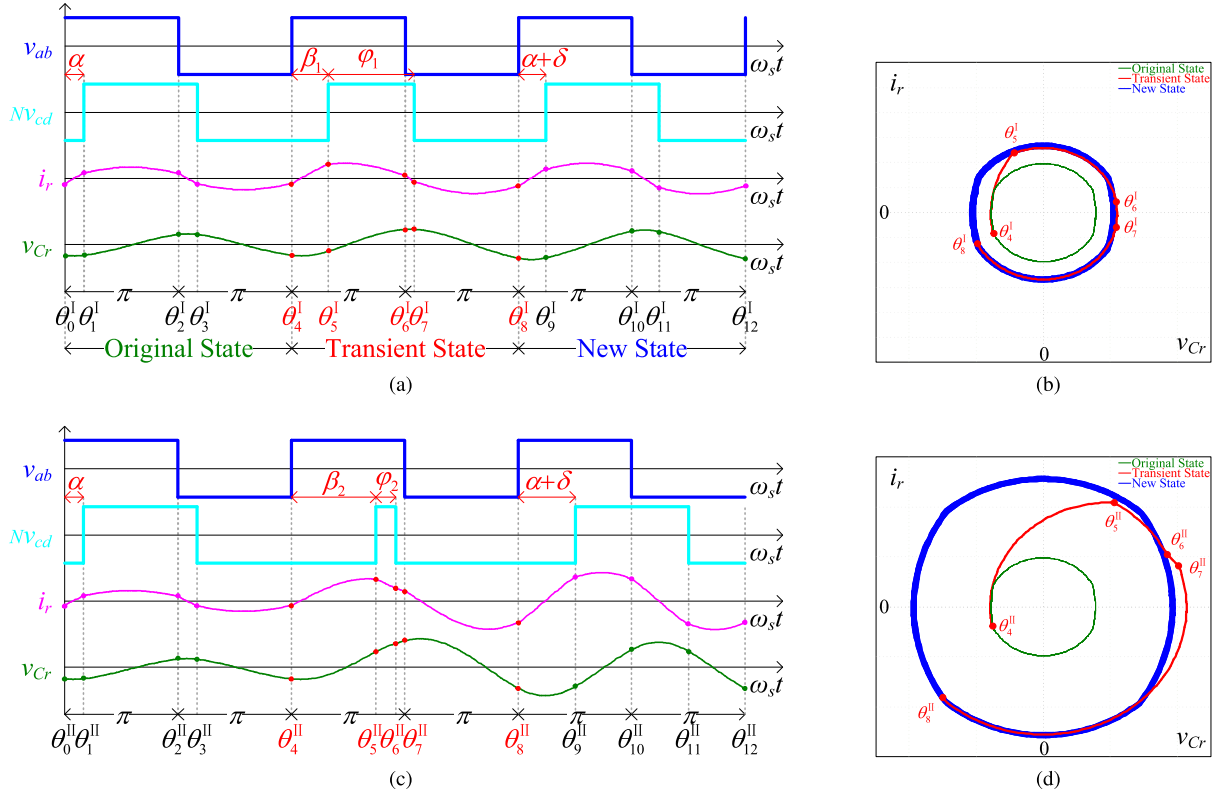


Fig. 7. Proposed TSM for  $\delta > 0$ . (a) Mode I. (c) Mode II. 2-D state-plane diagrams under TSM ( $\delta > 0$ ). (b) Mode I. (d) Mode II.

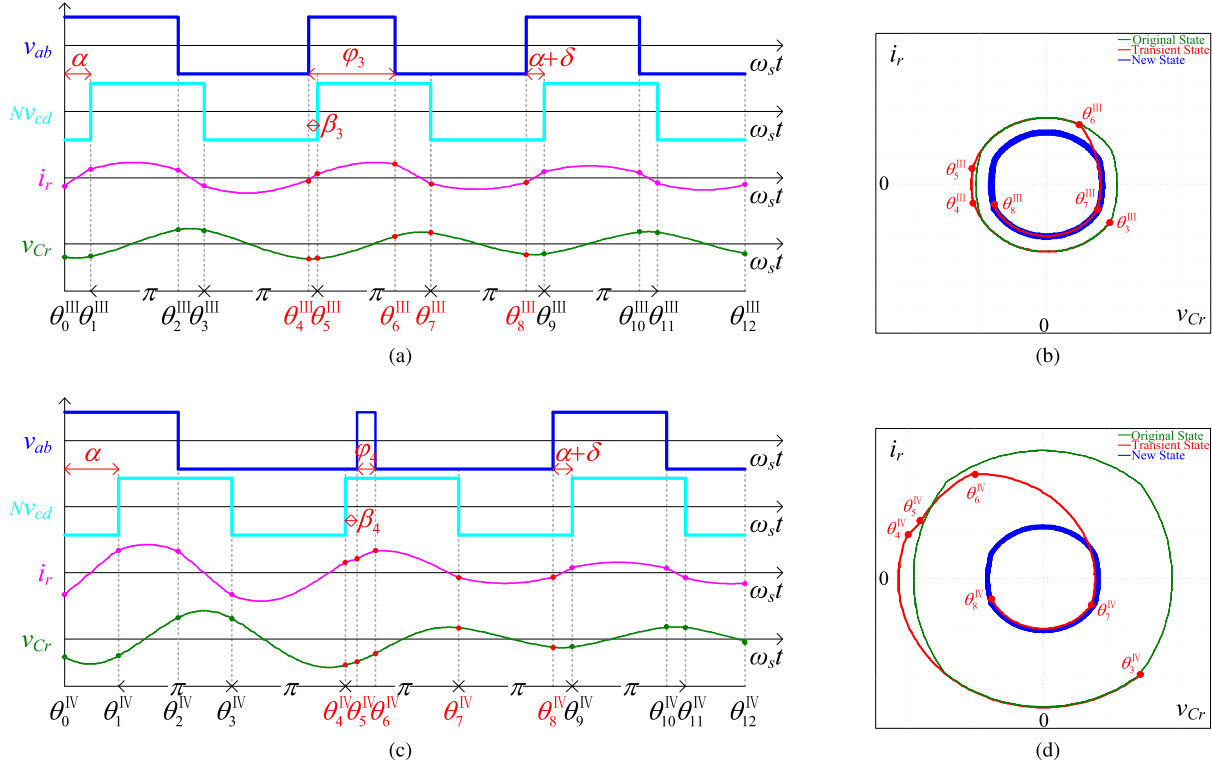


Fig. 8. Proposed TSM for  $\delta < 0$ . (a) Mode III. (c) Mode IV. 2-D state-plane diagrams under TSM ( $\delta < 0$ ). (b) Mode III. (d) Mode IV.

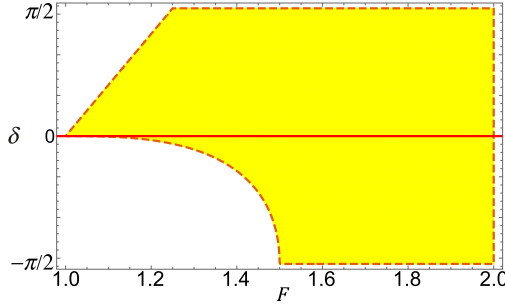


Fig. 9. Feasible solution region of (18).

Dividing (16) by (15) and simplifying the resulting equation leads to

$$\beta_1 = \frac{\pi + 2\alpha + \delta - \varphi_1}{2}. \quad (17)$$

Finally, substituting  $\beta_1$  from (17) into (15) or (16) yields

$$\varphi_1 = 2F \cdot \arcsin \left[ \frac{1}{2} \sec \left( \frac{\pi}{2F} \right) \sin \left( \frac{2\pi + \delta}{2F} \right) \right]. \quad (18)$$

Thus, (17) and (18) give the closed-form solutions for  $\varphi_1$  and  $\beta_1$  that satisfy the boundary conditions for producing oscillation-free transition from the original to the new steady states. It is evident that both  $\varphi_1$  and  $\beta_1$  are functions of  $F$ ,  $\alpha$ , and  $\delta$  only, which greatly simplifies the implementation of TSM as no sensing is required for other converter parameters, such as  $N$ ,  $V_1$ ,  $V_2$ ,  $i_r$ ,  $v_{Cr}$ , which are typically required by the existing trajectory control methods. The problems of high implementation complexity and high cost, which characterize the existing trajectory control methods, are thus overcome by the proposed TSM method. Finally, it should be noted that, although two operation modes are depicted in Fig. 7, there is no fundamental difference between them. This is evident from the above analysis, which does not distinguish the two operation modes in the mathematical derivation of (17) and (18); thus, the same equations are applicable to both operation modes, which again highlights the simplicity of the proposed method.

### B. Decreasing Power ( $\delta < 0$ )

The feasible solution region of (18) for  $\varphi_1 > 0$  is plotted in Fig. 9, where the dashed lines define the maximum allowable  $\delta$  in each execution of TSM. It can be seen that there is no feasible solution when  $\delta < 0$  and  $F$  is small, although the proposed method still works well for large  $F$ . To enlarge its feasible operating region, therefore, the proposed TSM method is modified as shown in Fig. 8(a) for  $\delta < 0$ , where the roles of  $v_{ab}$  and  $v_{cd}$  are reciprocated. With the modified TSM method, when power is decreased, i.e.,  $\delta < 0$ ,  $v_{cd}$  is kept unchanged as a 50% duty-cycle square wave at fixed frequency, while the positive pulse width  $\varphi_3$  of  $v_{ab}$  and the phase-shift angle  $\beta_3$  between  $v_{ab}$  and  $v_{cd}$  are modulated to eliminate HF transient oscillations during transient state. It can be shown that by following the same method of analysis as detailed in Section III-A, the solutions for  $\beta_3$  and  $\varphi_3$  can be determined as given by (19) and (20). Again, it should be noted that there is no fundamental difference between

the two operation modes, i.e., Mode III and Mode IV, depicted in Fig. 8; thus, the same equations are applicable to both operation modes.

$$\beta_3 = \frac{\pi - 2\alpha - \delta - \varphi_3}{2} \quad (19)$$

$$\varphi_3 = 2F \cdot \arcsin \left[ \frac{1}{2} \sec \left( \frac{\pi}{2F} \right) \sin \left( \frac{2\pi - \delta}{2F} \right) \right]. \quad (20)$$

### C. Unified Form of TSM

The following relationships can be summarized from Figs. 7 and 8:

- 1)  $\theta_5^I - \theta_3^I = (\pi - \alpha) + \beta_1$
- 2)  $\theta_9^I - \theta_7^I = \pi - (\beta_1 + \varphi_1 - \pi) + (\alpha + \delta)$
- 3)  $\theta_5^{II} - \theta_3^{II} = (\pi - \alpha) + \beta_2$
- 4)  $\theta_9^{II} - \theta_6^{II} = (\pi - \beta_2 - \varphi_2) + \pi + (\alpha + \delta)$
- 5)  $\theta_4^{III} - \theta_2^{III} = \alpha + (\pi - \beta_3)$
- 6)  $\theta_8^{III} - \theta_6^{III} = (\pi - (\varphi_3 - \beta_3)) + (\pi - (\alpha + \delta))$
- 7)  $\theta_5^{IV} - \theta_2^{IV} = \alpha + \pi + \beta_4$
- 8)  $\theta_8^{IV} - \theta_6^{IV} = (\pi - \beta_4 - \varphi_4) + (\pi - (\alpha + \delta))$ .

By combining the above relationships with (17) and (19),  $\beta_1$ ,  $\beta_2$ ,  $\beta_3$ , and  $\beta_4$  can be eliminated, thus resulting in

$$\begin{cases} \theta_5^I - \theta_3^I = \theta_9^I - \theta_7^I = (3\pi - \varphi_1 + \delta)/2 \\ \theta_5^{II} - \theta_3^{II} = \theta_9^{II} - \theta_6^{II} = (3\pi - \varphi_2 + \delta)/2 \\ \theta_4^{III} - \theta_2^{III} = \theta_8^{III} - \theta_6^{III} = (3\pi - \varphi_3 - \delta)/2 \\ \theta_5^{IV} - \theta_2^{IV} = \theta_8^{IV} - \theta_6^{IV} = (3\pi - \varphi_4 - \delta)/2 \end{cases} \quad (21)$$

which can be unified as

$$\begin{aligned} \theta_5^I - \theta_3^I &= \theta_9^I - \theta_7^I = \theta_5^{II} - \theta_3^{II} = \theta_9^{II} - \theta_6^{II} \\ &= \theta_4^{III} - \theta_2^{III} = \theta_8^{III} - \theta_6^{III} = \theta_5^{IV} - \theta_2^{IV} = \theta_8^{IV} - \theta_6^{IV} \\ &= (3\pi - \varphi + |\delta|)/2. \end{aligned} \quad (22)$$

Similarly, the pulselwidth  $\varphi$  of the transient-modulated square-wave voltage, i.e.,  $v_{ab}$  for  $\delta < 0$  and  $v_{cd}$  for  $\delta > 0$ , defined by (18) and (20), can be unified as

$$\varphi = 2F \cdot \arcsin \left[ \frac{1}{2} \sec \left( \frac{\pi}{2F} \right) \sin \left( \frac{2\pi + |\delta|}{2F} \right) \right]. \quad (23)$$

Consequently, a unified form of the proposed TSM method given by (22) and (23) is obtained, which is applicable to all four operation modes depicted in Figs. 7 and 8. Fig. 10 shows its implementation in a microprocessor by modifying the instantaneous values of the period (PRD) and counter-compare (CMP) registers and generating a floating triangular carrier signal during transient states.

Although the presented analysis and discussion focus on the case of forward power flow, the results are equally applicable to other cases, including increase/decrease of power in reverse power flow and reversal of power flow direction, as all these cases can be treated from the viewpoint of increasing or decreasing the phase-shift angle  $\delta$ . For example, when a DABSRC transitions from forward power flow to reverse power flow, a negative change of  $\delta$ , i.e.,  $\delta < 0$ , is involved, and such a scenario is readily handled by (19) and (20), or the unified equations (22) and (23).

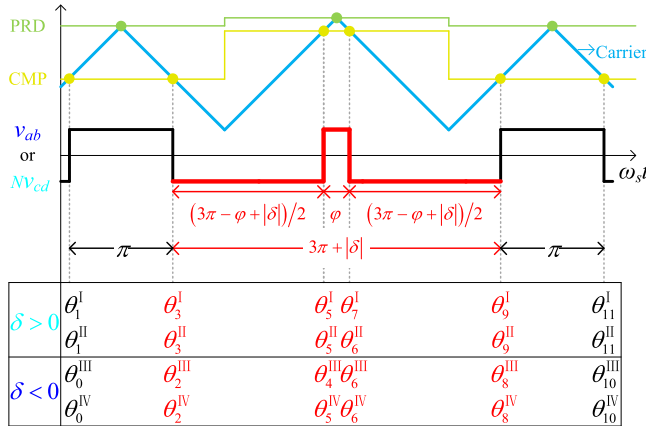


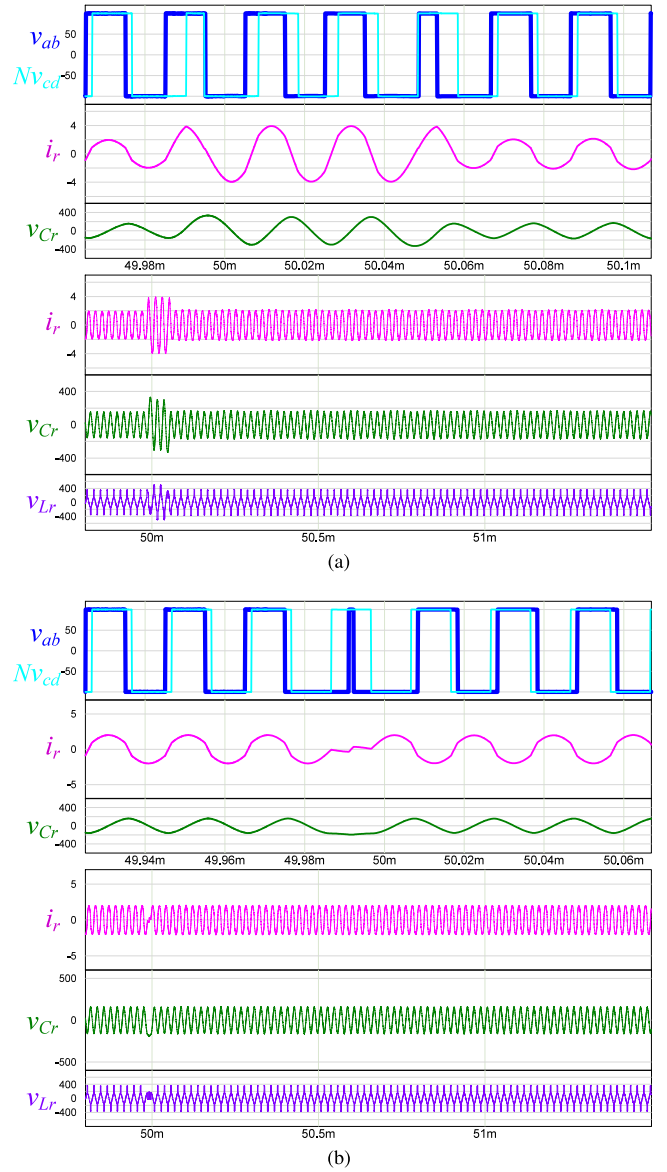
Fig. 10. Unified form of TSM and its switching processes.

To verify the effectiveness of the proposed TSM method, the open-loop transient responses of a DABSRC under TSM are simulated, and the results are presented in Fig. 11. To enable a fair comparison with the results shown in Fig. 5, the same converter parameters are used and the same cases involving both  $\delta > 0$  and  $\delta < 0$  are simulated. It is clear that, under the action of TSM, the transient resonant current  $i_r$  and resonant capacitor voltage  $v_{Cr}$  converge rapidly to their new steady-state values within one switching cycle without causing any visible HF transient oscillations. To verify this point, the transient state-plane diagrams of  $i_r$  and  $v_{Cr}$  for all three cases under CT-SPSM and TSM are plotted in Fig. 12 for a better visualization. It is clear from these plots that  $i_r$  and  $v_{Cr}$  under CT-SPSM generally undergo many cycles of oscillations before settling at their new steady-state trajectories, whereas  $i_r$  and  $v_{Cr}$  under TSM are seen to approach their new steady-state trajectories smoothly and directly with essentially no oscillations. Thus, the voltage and current stresses experienced by the converter's power stage components are significantly reduced, leading to a major improvement in their long-term reliability.

#### IV. MODEL PREDICTIVE CONTROL DESIGN FOR DABSRC

The block diagram of a typical closed-loop controlled DABSRC is shown in Fig. 13. The objective of the controller is to maintain a constant output voltage  $V_2$  in the presence of external disturbances, such as load variations, by modulating the phase-shift angle  $\alpha[n]$  between  $v_{ab}$  and  $v_{cd}$ . A PWM modulator is cascaded with the controller and is used to generate the required gating signals based on the controller's output, i.e., the target phase-shift angle, for realizing TSM or CT-SPSM.

In general, a high-gain controller leads to a smaller steady-state tracking error, but it also gives rise to a more abrupt and larger transient variation in  $\alpha[n]$ , which tends to produce undesirable large-amplitude HF transient oscillations when CT-SPSM is used. Consequently, CT-SPSM is only suitable for use with a low-gain controller, which will introduce only a small change in  $\alpha[n]$  in every switching cycle to produce a smooth but slow dynamic response of DABSRC. To evaluate

Fig. 11. Simulated transient responses under TSM. (a) Phase-shift angle is changed from  $\pi/6$  to  $\pi/3$  and back to  $\pi/6$ . (b) Phase-shift angle is changed from  $\pi/6$  to  $-\pi/6$ .

its practical advantages, therefore, TSM should be combined with a high-gain, fast controller such as MPC controller which will subject the TSM-based PWM modulator to more stringent operating requirements and thereby verifying its superiority in performance. MPC controller has recently been proven to be a powerful controller with fast reference tracking ability [6], [15], [16]. When applied to DABSRC, its main function is to determine an optimal phase-shift angle  $\alpha[n]$  that minimizes a cost function (e.g., output voltage tracking error) over a given prediction time horizon (e.g., one switching cycle) with the aid of the converter's dynamic model. In this section, an MPC controller will be designed for a DABSRC with the specifications given in Table I.

By using fundamental harmonic approximation (FHA) method [1], the transferred power  $P$  of a DABSRC can be

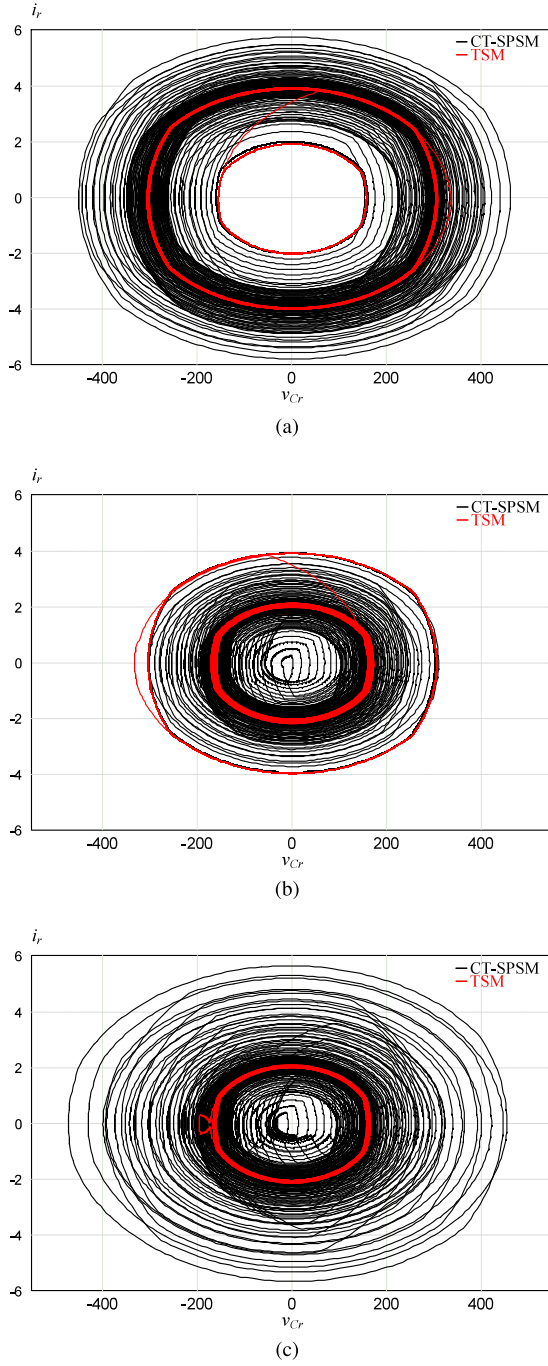


Fig. 12. Transient state-plane diagrams under CT-SPSM and TSM. (a)  $\alpha = \pi/6$ ,  $\delta = \pi/6$ , and  $\alpha + \delta = \pi/3$ . (b)  $\alpha = \pi/3$ ,  $\delta = -\pi/6$ , and  $\alpha + \delta = \pi/6$ . (c)  $\alpha = \pi/6$ ,  $\delta = -\pi/3$ , and  $\alpha + \delta = -\pi/6$ .

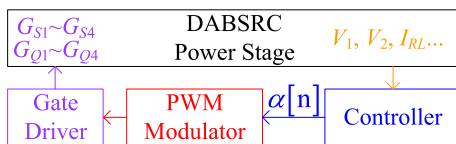


Fig. 13. Block diagram of a typical closed-loop controlled DABSR.

approximated by

$$P = \frac{1}{T_s} \int_0^{T_s} v_{ab}(t) i_r(t) dt \stackrel{\text{FHA}}{\approx} \frac{8NV_1 V_2 \sin \alpha}{\pi^2 X_r} \quad (24)$$

where  $X_r$  is the equivalent impedance of the series-resonant network.

At the output node in Fig. 1(a), a first-order differential equation (25) can be formulated that describes the dynamic behavior of  $V_2$ , where  $\bar{i}_2 = P/V_2$  is the average value of  $i_2$  over one switching period.

$$C_o \frac{dV_2}{dt} = \bar{i}_2 - I_{RL} = \frac{8NV_1 \sin \alpha}{\pi^2 X_r} - \frac{V_2}{R_L}. \quad (25)$$

Discretizing (25) by using forward Euler approximation yields (26), which can be used to predict the converter's output voltage at the next time step.

$$\begin{aligned} V_2[n+1] &= V_2[n] + V_2'[n]T_s \\ &= V_2[n] + \frac{8NV_1 \sin \alpha}{\pi^2 X_r C_{ofs}} - \frac{V_2[n]}{R_L C_{ofs}}. \end{aligned} \quad (26)$$

In order to accurately track the output reference voltage  $V_{2,\text{ref}}$  and minimize output voltage deviation, a quadratic cost function  $J$  can be introduced and formulated as  $J = [V_{2,\text{ref}} - V_2[n+1]]^2$ , which should be minimized to determine the optimal control variable (i.e., phase-shift angle) for the next time step. Based on the gradient descent method, the cost function  $J$  can be minimized when its gradient ( $\nabla J$ ) is equal to zero

$$\nabla J = 0. \quad (27)$$

Hence, the optimal phase-shift angle can be expressed as

$$\alpha[n+1] = \arcsin \left[ \frac{\pi^2 X_r C_{ofs}}{8NV_1[n]} \left[ V_{2,\text{ref}} - V_2[n] + \frac{V_2[n]}{R_L C_{ofs}} \right] \right]. \quad (28)$$

Then, the measured load current  $I_{RL}[n]$  can be used instead of the term  $\frac{V_2[n]}{R_L}$  in (28) to add a load-current feed-forward path for further enhancing dynamic response. This gives a modified expression of the predicted phase-shift angle  $\alpha[n+1]$

$$\alpha[n+1] = \arcsin \left[ \frac{\pi^2 X_r C_{ofs}}{8NV_1[n]} \left[ v_e[n] + \frac{I_{RL}[n]}{C_{ofs}} \right] \right] \quad (29)$$

where  $v_e[n] = V_{2,\text{ref}} - V_2[n]$  is defined as the error voltage.

Expanding (29) in a 1-D Taylor series around the steady-state operating point, and removing higher order nonlinear terms, leads to

$$\hat{\alpha} = W \left[ \hat{v}_e[n] + \frac{\hat{I}_{RL}[n]}{C_{ofs}} \right] \Big/ \sqrt{1 - \left[ W \left[ v_e[n] + \frac{I_{RL}[n]}{C_{ofs}} \right] \right]^2} \quad (30)$$

where  $W$  is given by  $W = \frac{\pi^2 X_r C_{ofs}}{8NV_1[n]}$ , and the symbol  $\hat{\cdot}$  denotes small-signal quantities.

However, the idealized equation (30) cannot be directly used for closed-loop control due to the HF noise associated with  $v_e$  and the presence of some unmodeled effects (e.g., power losses, sensing errors, power harmonics, etc.), which may affect the closed-loop regulation and even stability of the converter

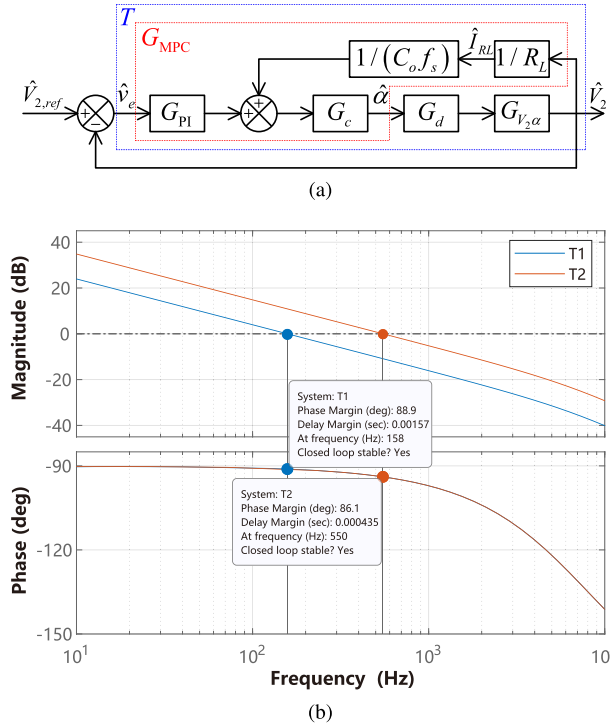


Fig. 14. Closed-loop design. (a) Overall control block diagram. (b) Bode plot of loop gain  $T(s)$ .

system. A PI compensator is required to compensate for the unmodeled effects as well as to act as a low-pass filter for attenuating HF noise and ensuring closed-loop stability. The overall transfer function of the MPC controller with the inclusion of PI compensator is therefore given by

$$G_{\text{MPC}}(s) = \frac{W \left[ \hat{v}_e[n] \left( K_p + \frac{K_i}{s} \right) + \frac{\hat{I}_{RL}[n]}{C_o f_s} \right]}{\sqrt{1 - \left[ \frac{W I_{RL}[n]}{C_o f_s} \right]^2}}. \quad (31)$$

Here, the proportional gain  $K_p$  plays a dominant role in determining the closed-loop performance of the converter, such as bandwidth, response speed, and stability. As discussed, some unmodeled effects always exist, thus an integral gain  $K_i$  should be included to eliminate steady-state error without significantly altering the dynamic properties of the converter.

Next, (25) is perturbed and linearized to yield the small-signal differential equation relating phase-shift angle  $\hat{\alpha}$  (i.e.,  $\delta$ ) and output voltage  $\hat{V}_2$

$$C_o \frac{d\hat{V}_2}{dt} = \frac{8N}{\pi^2 X_r} \left( V_1 \hat{\alpha} \cos \alpha + \hat{V}_1 \sin \alpha \right) - \frac{\hat{V}_2}{R_L}. \quad (32)$$

Taking the Laplace transform of (32) and setting  $\hat{V}_1 = 0$  yields the control-to-output transfer function  $G_{V_2\alpha}(s)$

$$G_{V_2\alpha}(s) = \frac{\hat{V}_2(s)}{\hat{\alpha}(s)} = \frac{8NV_1 R_L \cos \alpha}{\pi^2 X_r (1 + sC_o R_L)}. \quad (33)$$

Fig. 14(a) shows the overall control block diagram of the proposed MPC controller, where the transfer functions of the constituent blocks are defined as follows:

$$G_{\text{PI}}(s) = K_p + \frac{K_i}{s} \quad (34)$$

$$G_c(s) = W \sqrt{1 - \left[ \frac{W I_{RL}[n]}{C_o f_s} \right]^2} \quad (35)$$

$$G_d(s) = e^{-sT_d}. \quad (36)$$

Note that  $T_d$  is the inherent time delay introduced by the zero-order hold effect in digital implementation and  $G_d(s)$  represents its Laplace transform.  $G_c$  is the modulation gain relating error voltage to phase-shift angle.

Finally, the closed-loop transfer function of an MPC-controlled DABSRCS, i.e., transfer function from  $\hat{V}_{2,\text{ref}}(s)$  to  $\hat{V}_2(s)$ , is given by

$$G(s) = \frac{T(s)}{1 + T(s)} \quad (37)$$

where

$$T(s) = \frac{G_{\text{PI}}(s) G_c(s) G_d(s) G_{V_2\alpha}(s)}{1 - G_c(s) G_d(s) G_{V_2\alpha}(s) / (R_L C_o f_s)} \quad (38)$$

is the loop gain.

To verify the effectiveness of the proposed TSM method under different controller configurations, two sets of PI parameters are designed to yield two control loop bandwidths with a crossover frequency of 158 and 550 Hz, respectively, and the corresponding PI parameters are  $\{T_1: K_p = 0.02, K_i = 0.005\}$  and  $\{T_2: K_p = 0.07, K_i = 0.01\}$ . The bode plots of  $T_1$  and  $T_2$  are shown in Fig. 14(b). It can be seen that both controller configurations are well designed with abundant phase margins, i.e., of  $88.9^\circ$  for  $T_1$  and  $86.1^\circ$  for  $T_2$ , and hence good stability.

Additionally, TSM, which only operates during transient states, does not alter the pole locations prescribed by the controller, and hence does not affect the stability of the designed closed-loop DABSRCS. However, since it is unnecessary to trigger TSM when  $\delta$  is very small (as it will not give rise to large-amplitude transient oscillations), a minimum threshold  $\delta_{\text{th}}$  can be set below which TSM will not be triggered.

## V. SIMULATION AND EXPERIMENTAL VERIFICATION

The objective of this section is to validate the effectiveness of the proposed TSM under various dynamic conditions by comparing it to CT-SPSM. A scaled-down laboratory prototype, as shown in Fig. 15, has been constructed for the purpose. The hardware specifications and simulation parameters are listed in Table I. Two types of experiments are performed in this section: Open-loop and closed-loop, and their implementation flowcharts are shown in Fig. 16, where  $z^{-1}$  denotes a unit delay in  $z$ -Transform. Hence, the current phase-shift angle is  $\alpha[n] = z^{-1}\alpha[n+1]$  and the increment is  $\delta = \alpha[n+1] - \alpha[n]$ . For open-loop experiments [see Fig. 16(a)], no feedback loop is implemented and step changes in the phase-shift angle are

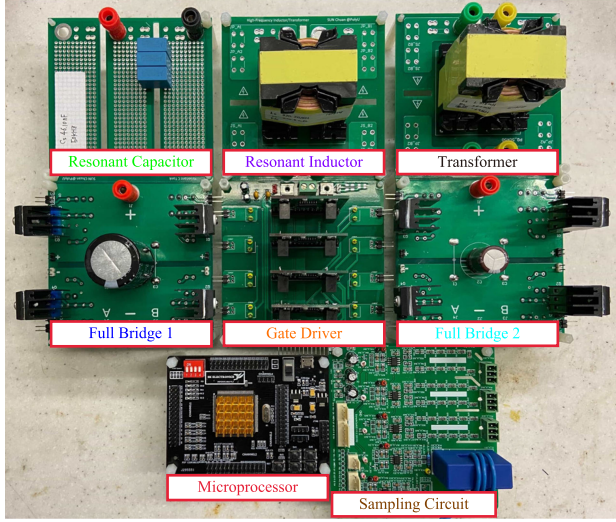


Fig. 15. Photograph of the experimental DABSRC prototype.

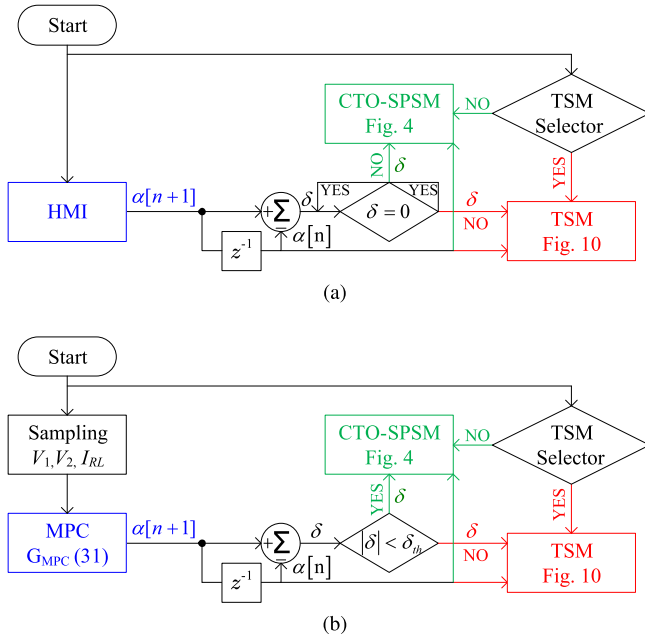


Fig. 16. Implementation flowcharts. (a) Open-loop configuration. (b) Closed-loop configuration.

directly applied to DABSRC through a human-machine interaction (HMI) software. When  $\delta \neq 0$ , the phase-shift angle is updated by CT-SPSM or TSM according to the decision of the “TSM Selector,” otherwise it waits for the next command. For closed-loop experiments [see Fig. 16(b)], the phase-shift angle is computed by the MPC controller designed in Section IV. As TSM should be activated during transient state only, a minimum  $|\delta| = \delta_{th}$  is defined above which TSM is activated, otherwise CT-SPSM is activated instead. It should be noted that, due to the finite bandwidth of the MPC controller, the rate of change of the phase-shift angle in closed-loop experiments is always slower than that in open-loop experiments; thus, it can be said

that open-loop experiments enable us to test the performances of CT-SPSM and TSM under extreme operating conditions involving abrupt and large-amplitude changes in the phase-shift angle.

### A. Open-Loop Tests

Fig. 17(a) and (b) shows the open-loop experimental transient responses of a DABSRC under CT-SPSM and TSM, respectively, when the phase-shift angle is increased from  $\pi/6$  to  $\pi/3$ . As can be seen from Fig. 17(a), under CT-SPSM, the resulting HF transient oscillations continue for approximately 40 cycles before  $i_r$  reaches the new steady state. More importantly, the original and the new steady-state amplitudes of  $i_r$  are 2.00 and 3.90 A, respectively, but its peak transient amplitude can reach as high as 5.70 A, leading to high current stress on the power stage components. On the contrary, as shown in Fig. 17(b),  $i_r$  reaches the new steady state in about one switching cycle under TSM without causing any visible transient oscillations.

Fig. 18 shows the measured transient responses when the phase-shift angle is decreased from  $\pi/3$  to  $\pi/6$ , while Fig. 19 shows the measured transient responses when the direction of power flow is reversed by changing the phase-shift angle from  $\pi/6$  to  $-\pi/6$ . Similar as before, with CT-SPSM,  $i_r$  suffers from severe HF transient oscillations under these conditions, resulting in peak transient current amplitudes that are significantly higher than the steady-state values. On the contrary, no visible transient oscillations are observed in the case of DABSRC under TSM as the trajectory of  $i_r$  has been planned to transit smoothly from the original to the new steady state in about one switching cycle.

As a result, it can be concluded that TSM has demonstrated an excellent performance in suppressing HF transient oscillations even under abrupt and large-amplitude changes in the phase-shift angle. This verifies its suitability for adoption in closed-loop design with fast controller such as MPC controller. The objective of the next subsection is to verify the performance of TSM under closed-loop conditions when regulated by an MPC controller.

### B. Closed-Loop Tests

In practice, DABSRC is generally operated in closed-loop configuration; therefore, the performance of TSM under closed-loop conditions is of greater practical interest and should be thoroughly verified. Thus, both simulation and experimental results are presented for a closed-loop DABSRC implemented with TSM. To highlight the merits of TSM, comparisons are made with a closed-loop DABSRC implemented with CT-SPSM. As discussed previously, MPC controller is selected as the feedback controller in these simulations and experiments due to its fast control action which is intended to introduce large-amplitude changes in the phase-shift angle when performing closed-loop regulation [16]. For all the simulations and experiments presented in this subsection, the output voltage of DABSRC is regulated by MPC controller under step-load changes between 1 and 2.2 A.

Figs. 20 and 21 show the simulated transient responses of DABSRC implemented with CT-SPSM and TSM for two sets

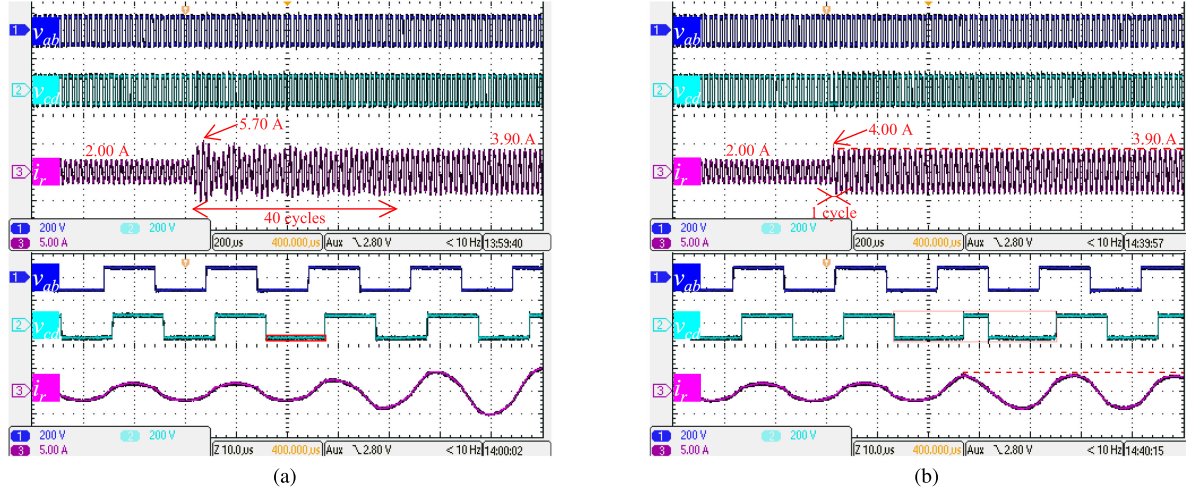


Fig. 17. Open-loop experimental results when the phase-shift angle is changed from  $\pi/6$  to  $\pi/3$ . (a) Under CT-SPSM [c.f. simulation results in Fig. 5(a)]. (b) Under TSM [c.f. simulation results in Fig. 11(a)].

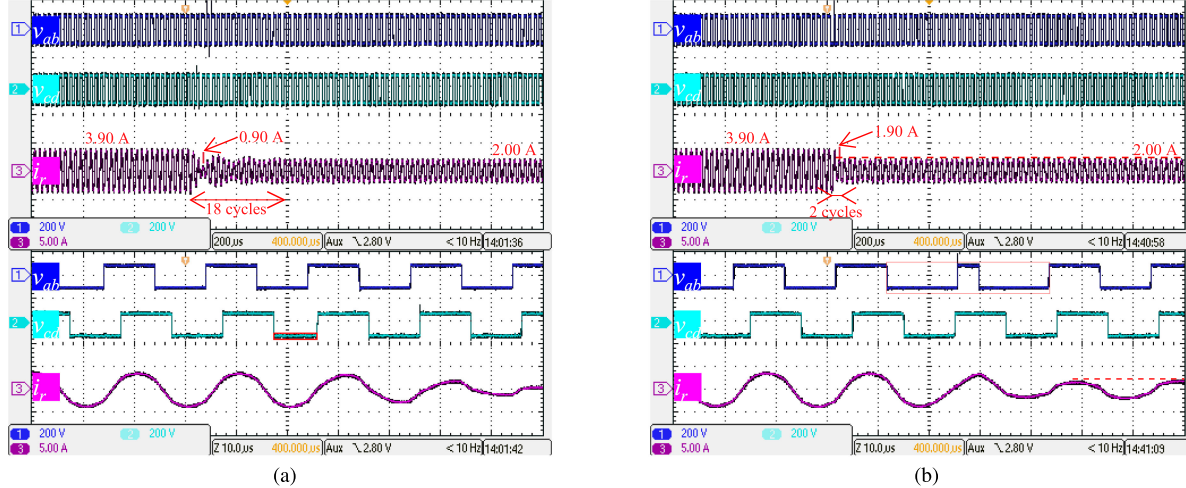


Fig. 18. Open-loop experimental results when the phase-shift angle is changed from  $\pi/3$  to  $\pi/6$ . (a) Under CT-SPSM [c.f. simulation results in Fig. 5(b)]. (b) Under TSM [c.f. simulation results in Fig. 11(a)].

of PI parameters. Fig. 20 corresponds to the slow-loop configuration  $T_1$ , whereas Fig. 21 corresponds to the fast-loop configuration  $T_2$ . As expected, it can be observed from these simulation results that DABSRCS under CT-SPSM generally suffers from severe HF transient oscillations during step-load changes, whereas DABSRCS under TSM exhibits no or only very weak transient oscillations during the same step-load changes as the trajectories of  $i_r$  and  $v_{Cr}$  are controlled by TSM to reach their new steady-state values rapidly. However, due to the inclusion of parasitic elements in the simulated DABSRCS which are not considered in the derivation of (23), there exists an incomplete suppression of HF transient oscillations by TSM in Figs. 20 and 21, leading to the existence of some small-amplitude residual oscillations in  $i_r$  and  $v_{Cr}$ . Another important observation is that, by comparing Figs. 20 and 21, faster control loop ( $T_2$ ) tends to cause more severe HF transient oscillations (i.e., higher transient peak amplitudes of  $i_r$  and  $v_{Cr}$ ) under CT-SPSM,

whereas the performance of TSM is less sensitive to control loop bandwidth as a result of the cycle-by-cycle planning of the trajectories of  $i_r$  and  $v_{Cr}$  in response to changes in the phase-shift angle.

Figs. 22 and 23 show the experimental results corresponding to the simulated cases depicted in Figs. 20 and 21. Generally, the experimentally measured transient responses under CT-SPSM and TSM for both slow-loop and fast-loop configurations match closely with the simulated transient responses. For CT-SPSM, a transient peak amplitude of 4.6 A is observed for  $i_r$ , i.e., 15% higher than the steady-state amplitude of 4.0 A, under step-load increase  $1 \text{ A} \rightarrow 2.2 \text{ A}$ , and it takes approximately 0.50 ms to reach the new steady state under the slow-loop configuration. Under the fast-loop configuration, the transient peak amplitude of  $i_r$  has increased to 7.2 A, i.e., 71% higher than the steady-state amplitude of 4.2 A, and it takes a much longer time (0.32 ms) to reach the new steady state. These observations again highlight

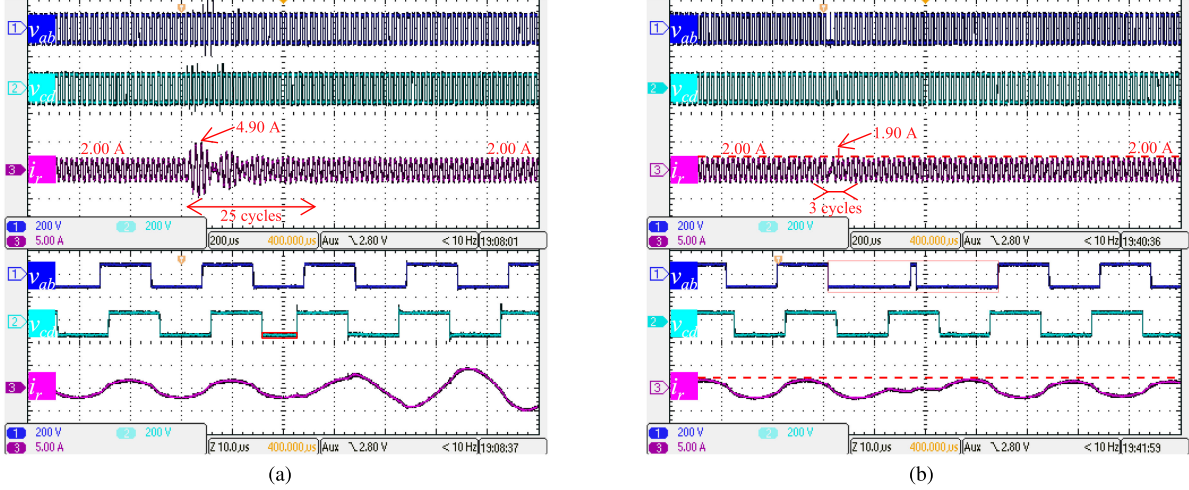


Fig. 19. Open-loop experimental results when the phase-shift angle is changed from  $\pi/6$  to  $-\pi/6$ . (a) Under CT-SPSM [c.f. simulation results in Fig. 5(c)]. (b) Under TSM [c.f. simulation results in Fig. 11(b)].

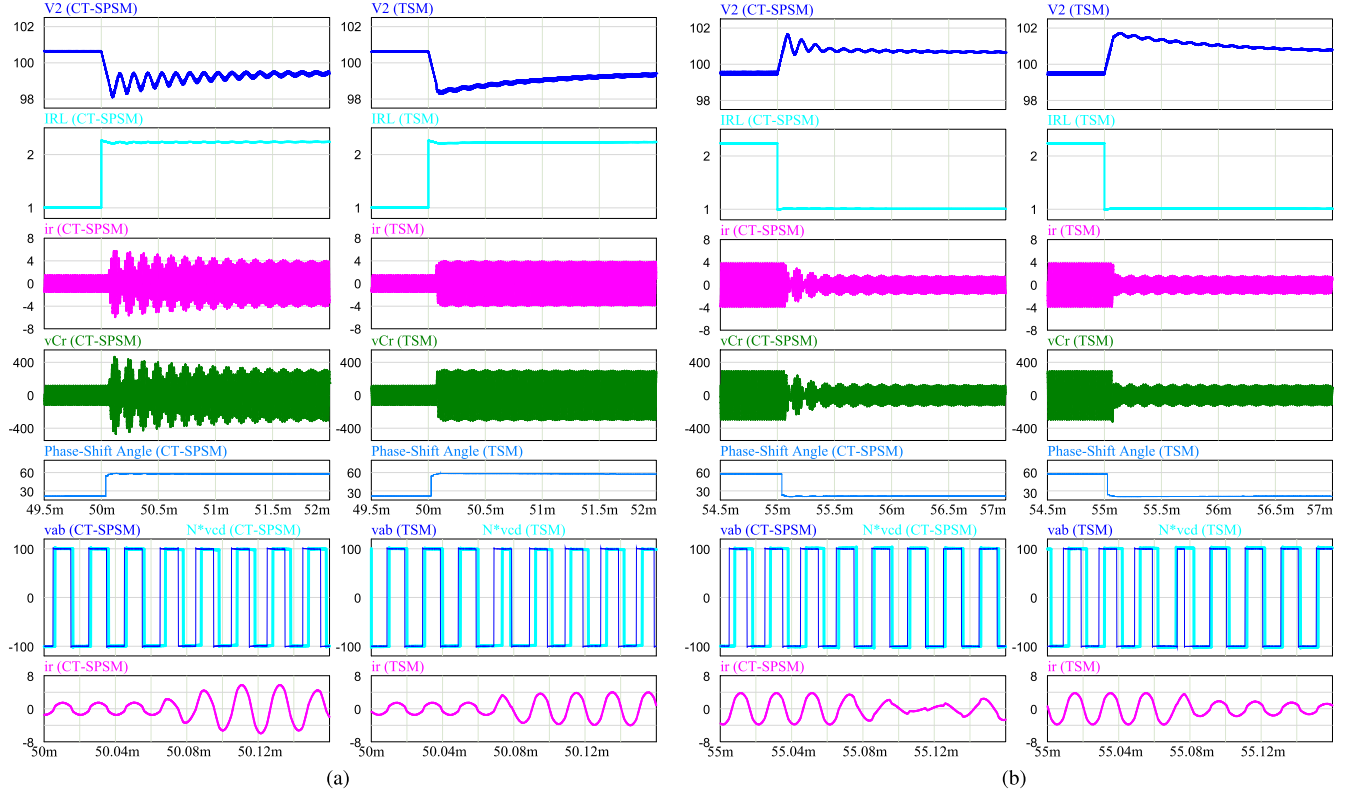


Fig. 20. Simulated step-load transient responses under MPC with  $T_1$  ( $K_p = 0.02$  and  $K_i = 0.005$ ). (a) Load step-up. (b) Load step-down.

the incompatibility of CT-SPSM with high-gain (fast) controller as it tends to introduce more severe HF transient oscillations as the control loop bandwidth increases and the phase-shift angle changes more rapidly. Under step-load decrease  $2.2 \text{ A} \rightarrow 1 \text{ A}$ , a severe undershoot is observed in  $i_r$  at the onset of transient response, and the degree of undershoot is observed to worsen with increasing control loop bandwidth, i.e., up to 1.3 A (72%) undershoot is resulted under the fast-loop configuration, to the

extent that large spikes are produced on the output voltage  $V_2$  leading to a degradation in the output voltage quality. These transient voltage spikes are associated with the loss of ZVS, as shown in Fig. 23(c), resulting from small phase-shift angles under MPC+CT-SPSM. For step-load decrease,  $i_r$  takes 0.24 ms and 0.22 ms, respectively, to reach the new steady state under the slow-loop and fast-loop configurations. It should be noted that the above observations also apply to  $v_{Cr}$  (since  $i_r = C_r \frac{dv_{Cr}}{dt}$ )

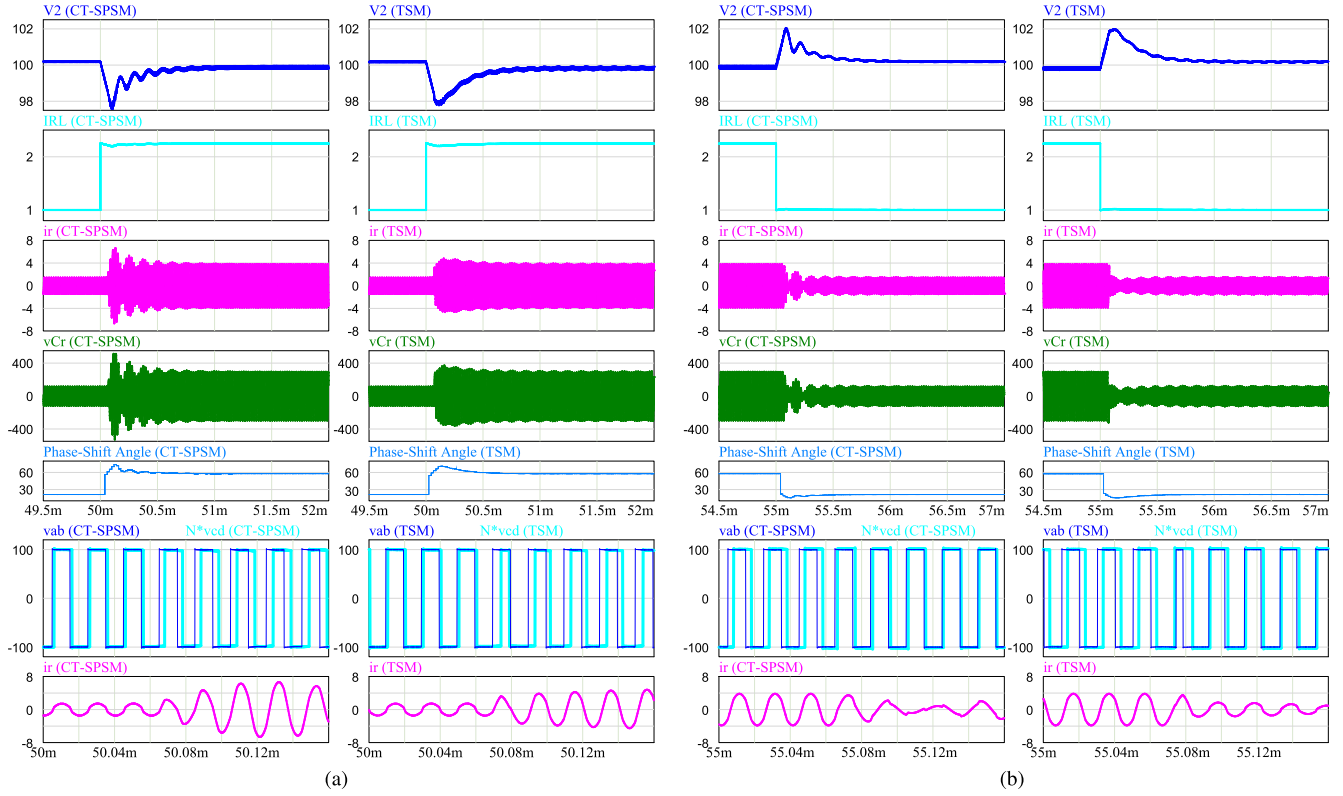


Fig. 21. Simulated step-load transient responses under MPC with  $T_2$  ( $K_p = 0.07$  and  $K_i = 0.01$ ). (a) Load step-up. (b) Load step-down.

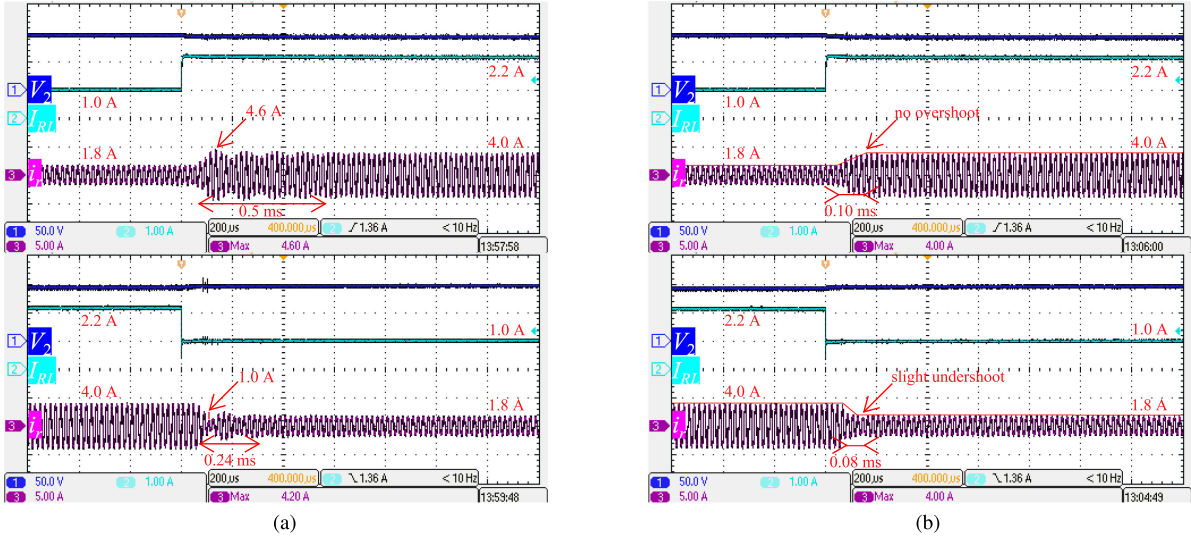


Fig. 22. Experimental step-load transient responses under (a) MPC+CT-SPSM and (b) MPC+TSM ( $T_1$ :  $K_p = 0.02$ ,  $K_i = 0.005$ ).

so the transient waveforms of  $v_{Cr}$  are omitted here due to space constraint.

On much the contrary, regardless of control loop bandwidth, no visible overshoot and undershoot are observed in  $i_r$  (as well as  $v_{Cr}$ ) during step-load increase and decrease when TSM is applied instead of CT-SPSM. For example, under the slow-loop configuration  $T_1$ ,  $i_r$  is observed to reach the new steady state

smoothly and rapidly in approximately 0.10 and 0.08 ms during step-load increase and decrease, i.e., 80% and 67% reduction compared to CT-SPSM, respectively. It is also observed that the settling time of  $i_r$  under TSM remains more or less the same for both slow-loop and fast-loop configurations, thus verifying the insensitivity of TSM's operation to controller configuration, making it ready for integration with any fast controller for

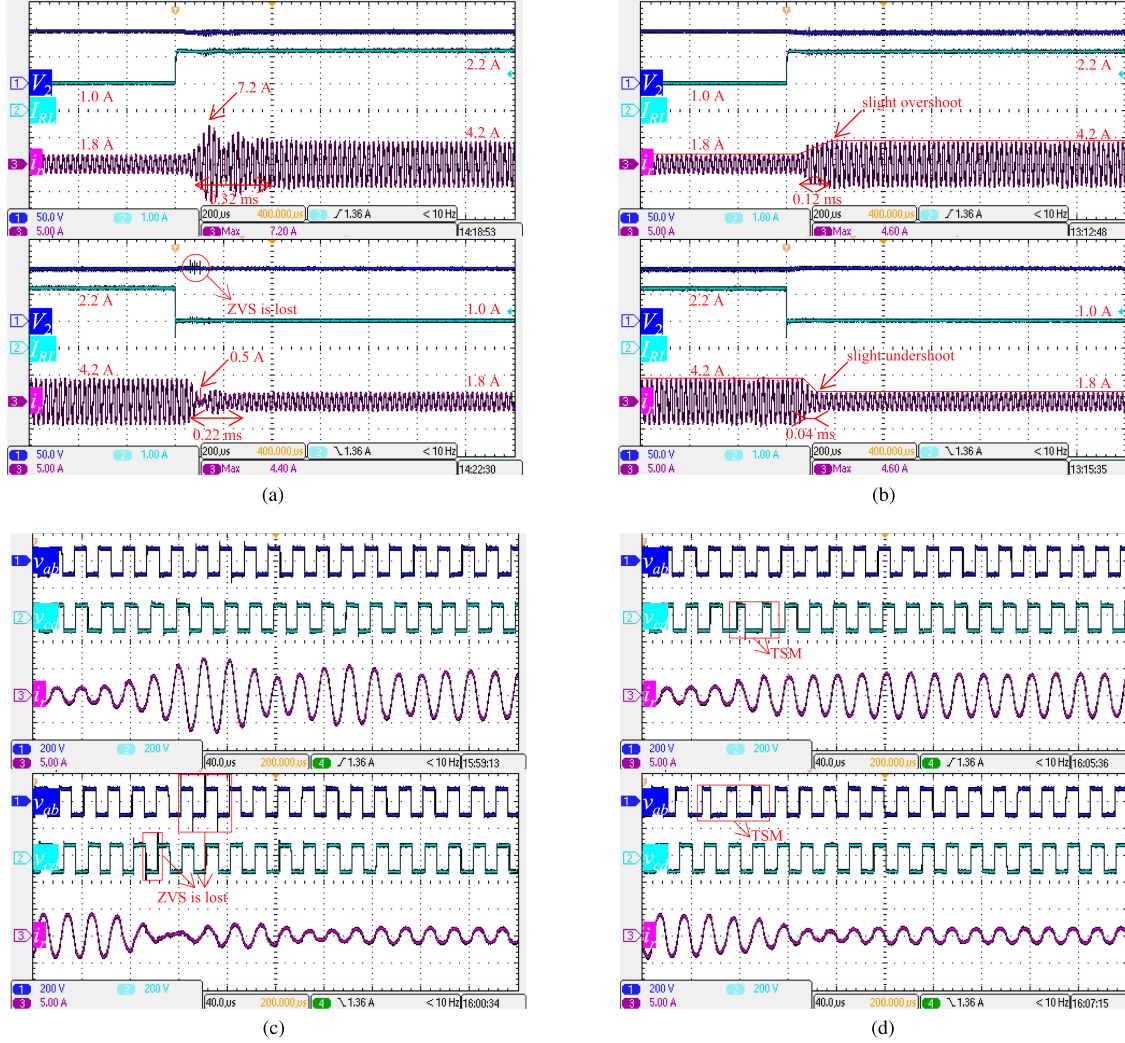


Fig. 23. Experimental step-load transient responses under (a) MPC+CT-SPSM and (b) MPC+TSM. Zoomed-in waveforms of  $v_{ab}$ ,  $v_{cd}$ , and  $i_r$  under (c) MPC+CT-SPSM and (d) MPC+TSM ( $T_2: K_p = 0.07$ ,  $K_i = 0.01$ ).

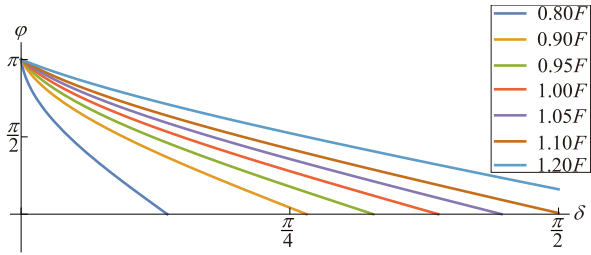
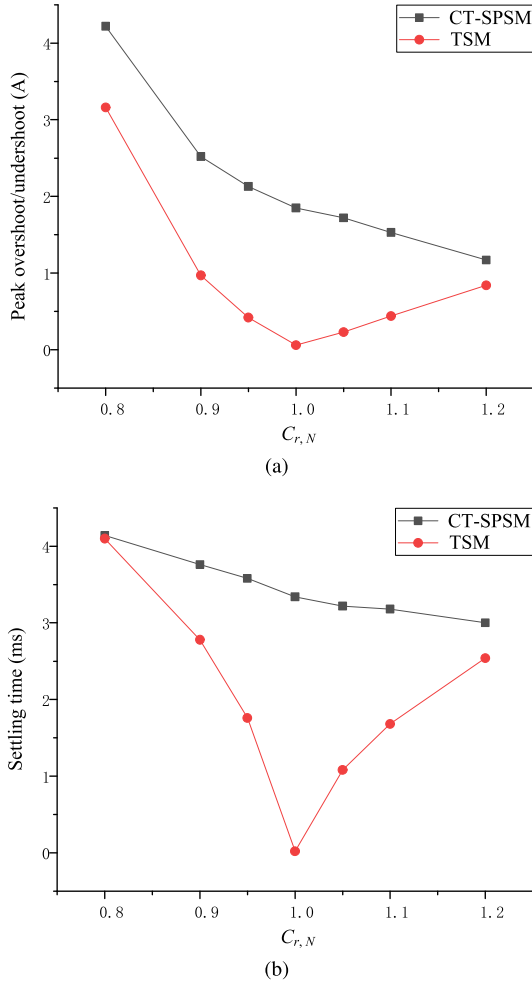
TABLE II  
PERFORMANCE COMPARISON OF CT-SPSM AND TSM UNDER  
OPEN-LOOP CONDITIONS

	Modulation	POS/PUS	ST
$\alpha = \pi/6$	Simulation	CT-SPSM	POS 1.85 A 167 cycles
		TSM	POS 0.06 A 001 cycle
$\delta = \pi/6$	Experiment	CT-SPSM	POS 1.80 A 040 cycles
		TSM	POS 0.10 A 001 cycle
$\alpha = \pi/3$	Simulation	CT-SPSM	PUS 1.63 A 134 cycles
		TSM	PUS 0.06 A 001 cycle
$\delta = -\pi/6$	Experiment	CT-SPSM	PUS 1.10 A 018 cycles
		TSM	PUS 0.10 A 002 cycles
$\alpha = \pi/6$	Simulation	CT-SPSM	POS 3.31 A 149 cycles
		TSM	PUS 0.07 A 001 cycle
$\delta = -\pi/3$	Experiment	CT-SPSM	POS 2.90 A 025 cycles
		TSM	PUS 0.10 A 003 cycles

realizing oscillation-free fast dynamic performance of DAB-SRC for many emerging power electronic applications requiring stringent bus voltage regulation, such as power supplies for data

TABLE III  
PERFORMANCE COMPARISON OF CT-SPSM AND TSM UNDER  
CLOSED-LOOP CONDITIONS

	Modulation	POS/PUS	ST
Load step-up transition under MPC with $T_1$	Simulation	CT-SPSM	POS 1.95 A 1.92 ms
	Experiment	TSM	POS 0.24 A 0.38 ms
Load step-down transition under MPC with $T_1$	Simulation	CT-SPSM	POS 0.60 A 0.50 ms
	Experiment	TSM	POS 0.00 A 0.10 ms
Load step-up transition under MPC with $T_2$	Simulation	CT-SPSM	PUS 1.30 A 0.84 ms
	Experiment	TSM	PUS 0.27 A 0.33 ms
Load step-down transition under MPC with $T_2$	Simulation	CT-SPSM	PUS 0.80 A 0.24 ms
	Experiment	TSM	PUS 0.20 A 0.08 ms
Load step-up transition under MPC with $T_2$	Simulation	CT-SPSM	POS 3.12 A 0.68 ms
	Experiment	TSM	POS 0.97 A 0.46 ms
Load step-down transition under MPC with $T_2$	Simulation	CT-SPSM	POS 3.00 A 0.32 ms
	Experiment	TSM	POS 0.40 A 0.12 ms
Load step-up transition under MPC with $T_2$	Simulation	CT-SPSM	PUS 1.33 A 0.43 ms
	Experiment	TSM	PUS 0.63 A 0.12 ms
Load step-down transition under MPC with $T_2$	Simulation	CT-SPSM	PUS 1.30 A 0.22 ms
	Experiment	TSM	PUS 0.20 A 0.04 ms

Fig. 24. Effect of variation in  $F$  on the feasible solution region of TSM.Fig. 25. Open-loop PSA results for an increase in phase-shift angle from  $\pi/6$  to  $\pi/3$ . (a) Peak overshoot/undershoot. (b) Settling time.

centers and electric vehicles. As exemplified in Fig. 23(d), the zoomed-in waveforms of  $v_{ab}$ ,  $v_{cd}$ , and  $i_r$  confirm the proper operation of TSM during transient states, indicating once again that the operation of TSM is decoupled from the actual controller configuration, thus providing greater flexibility in the design and implementation of fast controller for DABSRCS while ensuring the realization of oscillation-free transient responses in all cases.

To facilitate a comparison between CT-SPSM and TSM, all simulation and experimental results discussed above are

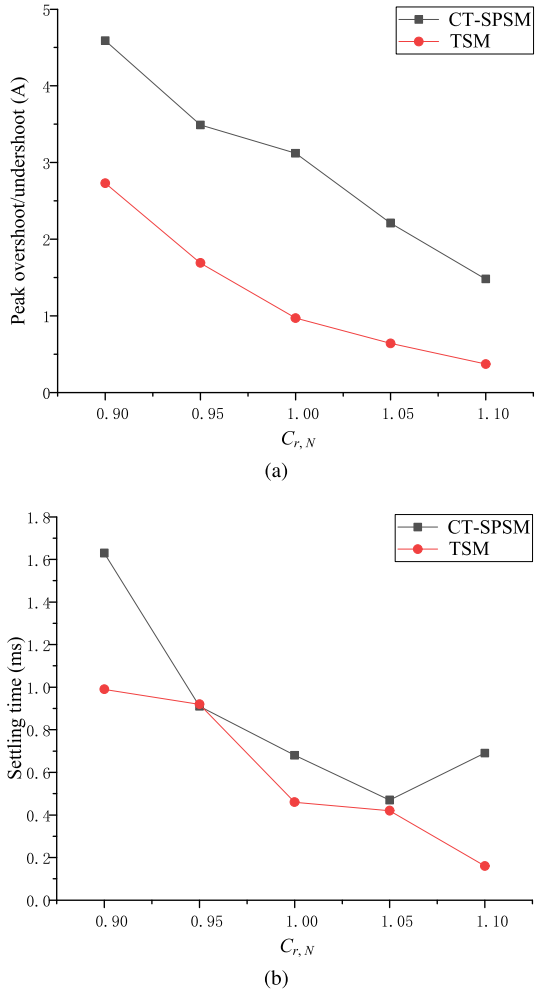


Fig. 26. Closed-loop PSA results for a step-load increase from 1 to 2.2 A. (a) Peak overshoot/undershoot. (b) Settling time.

summarized in Tables II and III. The main results are presented in the last two columns, where POS and PUS stand for “peak overshoot” and “peak undershoot,” respectively, and ST stands for “settling time.” It is evident from the tabulated results that the POS/PUS and ST associated with TSM are significantly lower compared to the figures associated with CT-SPSM, which confirms the effectiveness of TSM in suppressing HF transient oscillations and achieving fast convergence to new steady states. Except for a few cases, there is generally close agreement between the simulated and experimental results with the slight discrepancies predominantly due to parasitic components, parameter deviations, dead-time effects, power losses, etc.

### C. Parameter Sensitivity Analysis

In practice, the values of the resonant components can deviate from their nominal values due to manufacturing tolerances, temperature effects, component aging, etc. From (23), it can be seen that the transient modulation parameter  $\varphi$  is a function of the normalized frequency  $F$  ( $F = f_s/f_r$ ). Although  $f_s$  is constant for a fixed-frequency operated DABSRCS, variations in  $L_r$  and/or  $C_r$  can lead to changes in  $f_r$ , and hence  $F$ . To understand the

effect of variation in  $F$ , the feasible solution region of TSM for different  $F$  values are plotted in Fig. 24, from which it can be seen that the maximum allowable  $\delta$  in each execution decreases with decreasing  $F$ , implying that when this occurs the operation of TSM is limited to small step changes in phase-shift angle in each execution.

To further evaluate the performance of TSM under parameter variations, a detailed parameter sensitivity analysis (PSA) is performed, whereby the transient responses of DABSRC are simulated for different  $C_r$  under both open-loop and closed-loop conditions, and the corresponding POS/PUS and ST are recorded and plotted in Figs. 25 and 26, respectively. Fig. 25 depicts the open-loop PSA results for an increase in phase-shift angle from  $\pi/6$  to  $\pi/3$ , whereas Fig. 26 depicts the closed-loop PSA results for a step-load increase from 1 to 2.2 A, where  $C_{r,N}$  is defined as the normalized resonant capacitance with respect to the nominal capacitance. Despite the wide-range variation of  $C_r$ , it is evident that the POS/PUS and ST resulting from TSM remain consistently lower than those resulting from CT-SPSM, which confirms the effectiveness of TSM even after taking the effect of parameter variation into consideration.

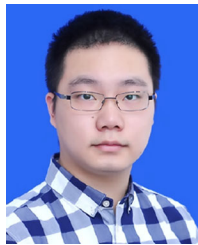
## VI. CONCLUSION

A new sensorless trajectory control method known as TSM is proposed to mitigate the problem of HF transient oscillations in DABSRC arising from CT-SPSM. As these HF transient oscillations typically take many switching cycles to decay before the converter reaches its new steady states, a truly fast dynamic response cannot be achieved by employing high-gain controller alone without considering the design of the underlying transient modulation strategy in parallel. In fact, it can be seen from Figs. 22 and 23, an inappropriately designed transient modulation strategy is likely to worsen the dynamic response of DABSRC, especially when a higher gain controller is employed. As demonstrated by both simulations and experiments, this study has shown that, by combining the proposed TSM method with a high-gain controller such as MPC controller, oscillation-free dynamic response can be readily achieved in DABSRC without requiring costly sensors and complex trajectory calculations, such that the transient peak-to-peak amplitude of resonant current is reduced and time-optimal transient performances can be obtained. This article represents the first attempt in the related literature to highlight the role of transient modulation and its importance in achieving high-quality and ultrafast dynamic response in DABSRC under both open-loop and closed-loop conditions. However, a limitation of the current study is that the proposed TSM strategy is only applicable to single-sided  $LC$ -type DABSRC, and more research effort is needed to generalize the proposed method to other topologies of the DAB converter family. In spite of this limitation, the insights gained from this article will lay the foundation for the future development of more advanced transient modulation strategies. In the future, efforts will be made to extend this concept to dual/triple-phase-shift modulation schemes and other variants of resonant DAB converters.

## REFERENCES

- [1] X. Li and A. K. Bhat, "Analysis and design of high-frequency isolated dual-bridge series resonant dc/dc converter," *IEEE Trans. Power Electron.*, vol. 25, no. 4, pp. 850–862, Apr. 2010.
- [2] L. Corradini, D. Seltzer, D. Bloomquist, R. Zane, D. Maksimović, and B. Jacobson, "Minimum current operation of bidirectional dual-bridge series resonant dc/dc converters," *IEEE Trans. Power Electron.*, vol. 27, no. 7, pp. 3266–3276, Jul. 2012.
- [3] M. Yaqoob, K. Loo, and Y. M. Lai, "A four-degrees-of-freedom modulation strategy for dual-active-bridge series-resonant converter designed for total loss minimization," *IEEE Trans. Power Electron.*, vol. 34, no. 2, pp. 1065–1081, Feb. 2019.
- [4] S. Hu, X. Li, and A. K. Bhat, "Operation of a bidirectional series-resonant converter with minimized tank current and wide ZVS range," *IEEE Trans. Power Electron.*, vol. 34, no. 1, pp. 904–915, Jan. 2019.
- [5] W. Han and L. Corradini, "Wide-range ZVS control technique for bidirectional dual-bridge series-resonant dc–dc converters," *IEEE Trans. Power Electron.*, vol. 34, no. 10, pp. 10256–10269, Oct. 2019.
- [6] L. Chen, S. Shao, Q. Xiao, L. Tarisciotti, P. W. Wheeler, and T. Dragievi, "Model predictive control for dual-active-bridge converters supplying pulsed power loads in naval dc micro-grids," *IEEE Trans. Power Electron.*, vol. 35, no. 2, pp. 1957–1966, Feb. 2020.
- [7] G. G. Koch *et al.*, "Design of a robust PI controller for a dual active bridge converter," in *Proc. 12th IEEE Int. Conf. Ind. Appl.*, 2016, pp. 1–6.
- [8] F. L. F. Marcelino, H. H. Sathler, T. R. de Oliveira, and P. F. Donoso-Garcia, "Modeling and control of a dual active bridge for energy storage in dc microgrid applications," in *Proc. IEEE 8th Int. Symp. Power Electron. Distrib. Gener. Syst.*, 2017, pp. 1–8.
- [9] Y. Pan *et al.*, "A dual-loop control to ensure fast and stable fault-tolerant operation of series resonant DAB converters," *IEEE Trans. Power Electron.*, vol. 35, no. 10, pp. 10994–11012, Oct. 2020.
- [10] H. Bai, C. Mi, C. Wang, and S. Gargies, "The dynamic model and hybrid phase-shift control of a dual-active-bridge converter," in *Proc. 34th Annu. Conf. IEEE Ind. Electron.*, 2008, pp. 2840–2845.
- [11] F. Krismer and J. W. Kolar, "Accurate small-signal model for the digital control of an automotive bidirectional dual active bridge," *IEEE Trans. Power Electron.*, vol. 24, no. 12, pp. 2756–2768, Dec. 2009.
- [12] D. Seltzer, L. Corradini, D. Bloomquist, R. Zane, and D. Maksimović, "Small signal phasor modeling of dual active bridge series resonant dc/dc converters with multi-angle phase shift modulation," in *Proc. IEEE Energy Convers. Congr. Expo.*, 2011, pp. 2757–2764.
- [13] S. Dutta, S. Hazra, and S. Bhattacharya, "A digital predictive current-mode controller for a single-phase high-frequency transformer-isolated dual-active bridge dc-to-dc converter," *IEEE Trans. Ind. Electron.*, vol. 63, no. 9, pp. 5943–5952, Sep. 2016.
- [14] Z. Shan, J. Jatskevich, H. H. Iu, and T. Fernando, "Simplified load-feedforward control design for dual-active-bridge converters with current-mode modulation," *IEEE Trans. Emerg. Sel. Topics Power Electron.*, vol. 6, no. 4, pp. 2073–2085, Dec. 2018.
- [15] F. An, W. Song, K. Yang, N. Hou, and J. Ma, "Improved dynamic performance of dual active bridge DC–DC converters using MPC scheme," *IET Power Electron.*, vol. 11, no. 11, pp. 1756–1765, 2018.
- [16] W. Song, M. Zhong, S. Luo, and S. Yang, "Model predictive power control for bidirectional series-resonant isolated dc–dc converters with fast dynamic response in locomotive traction system," *IEEE Trans. Transport. Electric.*, vol. 6, no. 3, pp. 1326–1337, Sep. 2020.
- [17] X. Li and Y.-F. Li, "An optimized phase-shift modulation for fast transient response in a dual-active-bridge converter," *IEEE Trans. Power Electron.*, vol. 29, no. 6, pp. 2661–2665, Jun. 2014.
- [18] B. Zhao, Q. Song, W. Liu, and Y. Zhao, "Transient DC bias and current impact effects of high-frequency-isolated bidirectional dc–dc converter in practice," *IEEE Trans. Power Electron.*, vol. 31, no. 4, pp. 3203–3216, Apr. 2016.
- [19] K. Takagi and H. Fujita, "Dynamic control and performance of a dual-active-bridge dc–dc converter," *IEEE Trans. Power Electron.*, vol. 33, no. 9, pp. 7858–7866, Sep. 2018.
- [20] R. Duan, L. Yuan, Q. Gu, J. Nie, and Z. Zhao, "Trajectory-prediction-based fast bidirectional power transient control for series resonant dual-active-bridge converter," in *Proc. IEEE Energy Convers. Congr. Expo.*, 2018, pp. 1415–1422.
- [21] R. Oruganti and F. C. Lee, "Resonant power processors, Part I-State plane analysis," *IEEE Trans. Ind. Appl.*, vol. IA- 21, no. 6, pp. 1453–1460, Nov. 1985.

- [22] R. Oruganti and F. C. Lee, "Resonant power processors: Part II—Methods of control," *IEEE Trans. Ind. Appl.*, vol. IA-21, no. 6, pp. 1461–1471, Nov. 1985.
- [23] R. Oruganti, J. J. Yang, and F. C. Lee, "Implementation of optimal trajectory control of series resonant converter," *IEEE Trans. Power Electron.*, vol. 3, no. 3, pp. 318–327, Jul. 1988.
- [24] W. Feng, F. C. Lee, and P. Mattavelli, "Simplified optimal trajectory control (SOTC) for LLC resonant converters," *IEEE Trans. Power Electron.*, vol. 28, no. 5, pp. 2415–2426, May 2013.
- [25] L. Rossetto, "A simple control technique for series resonant converters," *IEEE Trans. Power Electron.*, vol. 11, no. 4, pp. 554–560, Jul. 1996.
- [26] G. G. Oggier, M. Ordonez, J. M. Galvez, and F. Luchino, "Fast transient boundary control and steady-state operation of the dual active bridge converter using the natural switching surface," *IEEE Trans. Power Electron.*, vol. 29, no. 2, pp. 946–957, Feb. 2014.
- [27] S. Tian, F. C. Lee, and Q. Li, "A simplified equivalent circuit model of series resonant converter," *IEEE Trans. Power Electron.*, vol. 31, no. 5, pp. 3922–3931, May 2016.



**Chuan Sun** (Graduate Student Member, IEEE) received the B.Eng. degree in electronic and information engineering from the North University of China, Taiyuan, China, in 2015, and the M.Sc. degree in information technology from the Macau University of Science and Technology, Macau, China, in 2017. He is currently working toward the Ph.D. degree in power electronics with The Hong Kong Polytechnic University, Hong Kong, China.

From 2017 to 2018, he was an Electronic Engineer with Hangzhou Livoltek Power Co., Ltd., Hangzhou, China. His research interests include developing advanced modulation and control strategies for bidirectional dual-active-bridge dc–dc converters.



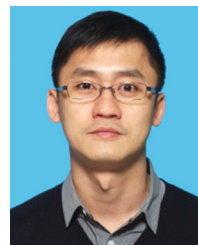
**Xingyue Jiang** is currently working toward the Ph.D. degree in electronic and information engineering with The Hong Kong Polytechnic University, Hong Kong, China.

His research interests include peer-to-peer energy trading, energy path planning, and energy Internet.



**Lingling Cao** (Member, IEEE) received the B.S. and M.S. degrees in electrical engineering from the Nanjing University of Aeronautics and Astronautics, Nanjing, China, in 2008 and 2011, respectively, and the Ph.D. degree from The Hong Kong Polytechnic University, Hong Kong, China, in 2015.

She is currently an Assistant Professor with the Harbin Institute of Technology, Shenzhen, China. Her research interests include power converter topologies and control strategies for renewable energy systems.



**K. H. Loo** (Member, IEEE) received the B.Eng. (Hons.) and Ph.D. degrees in electronic engineering from the University of Sheffield, Sheffield, U.K., in 1999 and 2002, respectively.

From 2002 to 2004, he was in the Japan Society for the Promotion of Science Postdoctoral Fellow with Ehime University, Matsuyama, Japan. Since 2006, he has been with The Hong Kong Polytechnic University, Hong Kong, China, where he is currently an Associate Professor with the Department of Electronic and Information Engineering. His research interests include power electronics for renewable energy systems.

Dr. Loo has been an Associate Editor for the *IEEE TRANSACTIONS ON ENERGY CONVERSION* since 2013 and *IEEE Open Journal of Circuits and Systems* since 2019, and a Reviewer for various international journals and conferences. He is currently the Chair of the Power Electronics and Control Sub-Committee of the IEEE Technical Committee on Transportation Electrification.